



저작자표시-비영리-변경금지 2.0 대한민국

이용자는 아래의 조건을 따르는 경우에 한하여 자유롭게

- 이 저작물을 복제, 배포, 전송, 전시, 공연 및 방송할 수 있습니다.

다음과 같은 조건을 따라야 합니다:



저작자표시. 귀하는 원저작자를 표시하여야 합니다.



비영리. 귀하는 이 저작물을 영리 목적으로 이용할 수 없습니다.



변경금지. 귀하는 이 저작물을 개작, 변형 또는 가공할 수 없습니다.

- 귀하는, 이 저작물의 재이용이나 배포의 경우, 이 저작물에 적용된 이용허락조건을 명확하게 나타내어야 합니다.
- 저작권자로부터 별도의 허가를 받으면 이러한 조건들은 적용되지 않습니다.

저작권법에 따른 이용자의 권리는 위의 내용에 의하여 영향을 받지 않습니다.

이것은 [이용허락규약\(Legal Code\)](#)을 이해하기 쉽게 요약한 것입니다.

[Disclaimer](#)

Master's Thesis

Highly improved cycling stability of a large-sized
LiCoO₂ cathode material at 4.5 V via high
temperature solid-state surface modification

Youngbin You

Department of Energy Engineering
(Battery Science and Technology)

Graduate School of UNIST

2019

Highly improved cycling stability of a large-sized
LiCoO₂ cathode material at 4.5 V via high
temperature solid-state surface modification

Youngbin You

Department of Energy Engineering
(Battery Science and Technology)

Graduate School of UNIST

Highly improved cycling stability of a large-sized
LiCoO₂ cathode material at 4.5 V via high
temperature solid-state surface modification

A thesis
submitted to the Graduate School of UNIST
in partial fulfillment of the
requirements for the degree of
Master of Science

Youngbin You

12. 05. 2018

Approved by



Advisor

Jaephil Cho

Highly improved cycling stability of a large-sized
LiCoO₂ cathode material at 4.5 V via high
temperature solid-state surface modification

Youngbin You

This certifies that the thesis of Youngbin You is approved.

12. 05. 2018



Advisor: Jaephil Cho



Kyeong-Min Jeong



Nam-Soon Choi

Abstract

Pushing a cut-off voltage higher is one of the best approaches to enhance both the capacity and energy density of the conventional LiCoO_2 cathode. However, charging the LiCoO_2 cells repeatedly to voltages higher than 4.35 V versus Li/Li^+ induces significant degradations in the surface and bulk structure, which eventually leads to the severe capacity fading. This has spurred intensive research efforts to enhance the cycling stability of the LiCoO_2 cathode at high voltages over the past decade, including the surface coating and bulk doping methods. Nevertheless, most approaches showed only partially improved structural and surficial stability and thus practical reversible capacity of the LiCoO_2 is still limited. In this work, we review previous studies on degradation mechanisms of the layered cathode materials at high voltages and strategies to improve their cycling stability. Furthermore, we also reveal that the degradation of the large-sized LiCoO_2 cathode material was mainly due to the significant crack formation and irreversible structural changes. On the basis of this finding, we demonstrate that a high temperature solid-state surface modification method via coating materials can be a great practical approach to enhance the cycling stability of the LiCoO_2 cells. This simple, one-step strategy can not only enhance the reversibility of the bulk phase transition and surface stability of the LiCoO_2 , but also effectively suppress the crack formation. The modified LiCoO_2 exhibits a highly stable cycling stability in the full-cell system with a capacity retention of $\sim 87\%$ after 500 cycles at room temperature.

Contents

Abstract

List of Figures

List of Tables

I. Introduction-----	1
1.1 Layered LiCoO ₂ cathode material-----	3
1.2 High voltage operation of layered cathode materials-----	4
1.2.1 Degradation mechanisms of layered cathode materials in high voltage environment-----	6
1.2.2 Previous strategies for high voltage operation of layered cathode materials-----	14
1.2.3 Objective of this work-----	19
II. Experimental detail-----	20
III. Results and discussion	
3.1 Morphology, structure, and surface composition-----	22
3.2 Electrochemical results-----	28
3.3 Structural analysis-----	35
IV. Conclusion-----	50
References-----	51

List of Figures

Figure 1. (a) Energy storage systems (ESSs) utilizing various energy sources. (b) The duration and power of various ESSs.

Figure 2. (a) Crystal structure of the LiCoO_2 . (b) Octahedral CoO_6 structure. (c) ABCABC stacking arrangement of the LiCoO_2 .

Figure 3. A scheme showing the electrochemical voltage window of an electrolyte.

Figure 4. (a) Nucleophilicity of the oxygen at the delithiated cathode surface with the atomic number of transition metal. (b) Nucleophilic attack at the surface of layered oxide and EC decomposition.

Figure 5. (a) Illustrations showing the effects of the nanostructured stabilizer which can suppress nickel ion dissolution of the NCM ($\text{LiNi}_{0.8}\text{Co}_{0.1}\text{Mn}_{0.1}$). Ni 2p X-ray photoelectron spectroscopy (XPS) spectra of the graphite anode in the (b) NCM/graphite full-cell and (c) NS-NCM/graphite full-cell after the cycling. Nanostructured stabilizer-incorporated NCM was denoted as NS-NCM. More Ni^{2+} ions were detected on the anode surface of the NCM/graphite full-cell.

Figure 6. (a) Differential capacity vs. voltage curves of the LiCoO_2 (LCO) cell charged to 4.6 V for different cycles, which shows the irreversible phase transition of the LCO at high cut-off voltage. (b) Phase diagram of Li_xCoO_2 according to the Li contents ($0 < x < 1$).

Figure 7. HADDF-STEM images of the NMC333 surface. (a) Pristine sample, (b) after 100 cycles with a cut-off voltage of 4.2 V, and (c) after 100 cycles with a high cut-off voltage of 4.8 V. (d) Magnified STEM image from the red box in (c). The insets are the models illustrating lattice change from the surface into the bulk, where transition metal, oxygen, and Li ions are denoted by blue, red, and green balls, respectively. The surface reconstruction layer was indicated by yellow dashed lines. Fast Fourier transformation (FFT) patterns from each region in (d) are shown, where blue arrows indicate migrated TM ions and dashed black frames show the unit cell of three different regions.

Figure 8. (a) A graph and high angle annual dark field (HAADF) images illustrating the relationship between the degree of intragranular cracks and cycling voltage. (b) Schemes for crack incubation and propagation process assisted by the dislocation. (c) A crack-propagation process, accompanying the oxygen loss and phase transformation.

Figure 9. (a) A schematic showing the mechanism of AlPO_4 coating on the LiCoO_2 cathode material, resulting structure and composition. (b) Surface TEM images of the “ AlPO_4 ”-coated LiCoO_2 . (c) Electrochemical performance of the bare LiCoO_2 and “ AlPO_4 ”-coated LiCoO_2 for 30 cycles. Voltage ranged from 3.0 to 4.7 V and charge/discharge C rate was C/5, except for the first cycle (C/10).

Figure 10. (a) In-situ XRD results of the LiNiO_2 , LiCoO_2 , and $\text{LiCo}_{0.9}\text{Ni}_{0.1}\text{O}_2$ (black, red, and green pattern, respectively) during charging process. (b) Voltage profiles of the LiCoO_2 and $\text{LiCo}_{0.9}\text{Ni}_{0.1}\text{O}_2$ during 20 cycles between 3.0 and 4.5 V. (c) A scheme showing phase transition and change in lattice

parameter c during charging process.

Figure 11. SEM images of the (a) LCO and (b) M-LCO.

Figure 12. Powder XRD results of the LCO and M-LCO.

Figure 13. A scanning transmission electron microscopy (STEM) image and EDX mapping data of the M-LCO surface.

Figure 14. (a) A high angle annual dark field (HAADF)-STEM image of the M-LCO surface and (b) corresponding EDX spectrum results of each region in (a).

Figure 15. (a) A magnified STEM image and EDX line scanning of the M-LCO surface. The inset is the signal of P K series. (b) EDX point scanning from white dot region and mapping data, indicating agglomerating of P at the surface.

Figure 16. A magnified HR-TEM images of the (a) LCO and (b) M-LCO. Magnified STEM images of the outer (site A) and inner (site B) surface and corresponding FFT patterns are also shown.

Figure 17. Electrochemical performance (half-cell) of the LCO and M-LCO (voltage range: 3.0 to 4.5 V). (a), (d) The voltage profile graph of the formation cycle at 25 °C and 60 °C. Charge and discharge C-rate was 0.1C. (b), (c) The cycle performance at 25 °C and 60 °C (charge and discharge C-rate: 0.5 and 1C, respectively).

Figure 18. $dq \, dV^{-1}$ curves of 1st, 10th, 25th, 50th cycle for the (a) LCO and (b) M-LCO.

Figure 19. (a) Rate capability test of the LCO and M-LCO. Constant charge C rate (0.2C) was applied and discharge C rate was increased from 0.2 to 5.0C every four cycles. (b) EIS measurements of the LCO and M-LCO recorded after the formation, 25th, and 50th cycle.

Figure 20. Voltage profile of GITT for the LCO and M-LCO after the (a) formation and (b) 50th cycle. (c) Change in values for IR drop and overpotential at various state of charge (SOC) from 10% to 90%.

Figure 21. Electrochemical performance of the LCO and M-LCO in the full cell configuration. Artificial graphite was used for the anode. (a) Voltage profile graph at the formation cycle. (b) Cycle performance and (c) coulombic efficiency data during 500 cycles. (d) Change in voltage profile of the LCO and M-LCO during 100 and 500 cycles, respectively.

Figure 22. The contents of Co ions in the electrolyte for the LCO and M-LCO after the storage at 60 °C for 4 weeks, measured by ICP.

Figure 23. The EDS mapping and spectrum data of the (a) LCO and (b) M-LCO cathode after full cell test. The quantification data was also included.

Figure 24. SEM images of the (a) LCO and (b) M-LCO cathode composite after full cell 500 cycles.

Figure 25. Micro and atomic structure of the LCO surface after cycling. (a) TEM images of the LCO after full-cell 500 cycles. (b) A HR-TEM image of the LCO surface. (c) A STEM image of the white box in (b). The insets are FFT patterns of the region 'A' and 'B'.

Figure 26. Surface micro and atomic structure of the M-LCO after cycling. (a) TEM images of the M-LCO after full-cell 50 cycles. (b) A HR-TEM image of the M-LCO surface. (c) Outermost STEM

image in (b). The inset is the FFT pattern of the surface in (c). (d) A bright-field (BF) STEM image of the (c).

Figure 27. (a) A TEM image showing the large microcrack in the cycled LCO. (b) A magnified TEM image of the white box in (a). (c) A magnified HR-TEM image of the white box in (b). The white arrows indicate different Li ion diffusion pathway in each broken particle. The insets are FFT patterns from each separated particle.

Figure 28. Micro and atomic structure of the LCO near the cracks. (a) A TEM image of the LCO after cycling. The red ellipse indicates the broken interface of the particle that the crack formed. (b) A HR-TEM image of the white box in (a). (c), (d) STEM images of the white box ‘A’ in (b). (e) A STEM image of the white box ‘B’ in (b). (f) FFT patterns in region ‘C’ and ‘D’ in (e).

Figure 29. Change in XRD peaks of the LCO and M-LCO after cycling.

Figure 30. The SEM images of the graphite anode in the (a) LCO/Gr and (b) M-LCO/Gr full cell after 500 cycles. The cross-sectional SEM images and EDS mapping data (right side) was presented. In the mapping image, blue and green signals indicate the carbon and Co element, respectively.

Figure 31. The EDS mapping and spectrum data of the graphite anode in the (a) LCO/Gr and (b) M-LCO/Gr full cell after the 500 cycles. The quantification data was also presented.

Figure 32. (a) Voltage profiles of the reassembled LCO and M-LCO cathode in half-cell after full-cell 500 cycles (voltage range: 3.0 to 4.5 V). (b) Voltage profiles of the reassembled graphite anode half-cell in the voltage ranged from 0.005 to 1.5 V. Fresh electrolyte and lithium metal were used for the reassembly and all the reassembled half-cells were charged and discharged 25 times at 0.1C.

Figure 33. The SEM images (BSE mode) of the separator in the (a) LCO/Gr and (c) M-LCO/Gr full-cell after the 500 cycles. (b) EDS mapping image for the separator in the LCO/Gr full cell.

List of Tables

Table 1. Physical properties of the LCO and M-LCO.

Table 2. Charge transfer resistance of the LCO and M-LCO.

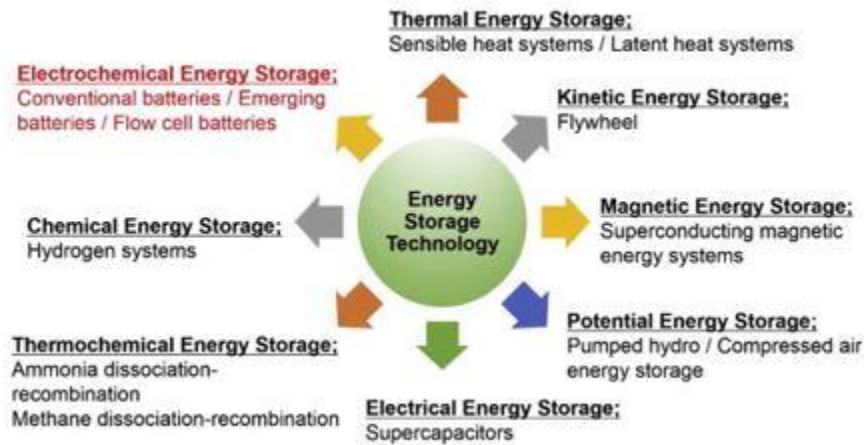
Table 3. Loss of Co from the LCO and M-LCO after storage test.

I. Introduction

Today, the development of renewable energy has become a global issue because of worldwide energy regulations to reduce the use of fossil fuel. However, for the utilization of this energy source in real life, we need to develop not only energy conversion technologies, but also good energy storage systems (ESSs). There are various types of ESS utilizing electrochemical energy, thermal energy, kinetic and potential energy. Among them, systems using electrochemistry (such as batteries) are receiving the most attention because of their advantages in price, efficiency, and application (Figure 1).¹⁻² The electrochemical energy storage system has rapid energy conversion because the electrical energy is directly converted by electrochemical oxidation and reduction reactions. To date, rechargeable lithium-ion batteries (LIBs) are the best candidates for electrochemical ESS in terms of practical gravimetric/volumetric energy density, storage capability at high rates, space/size limitations, operating potential/coulombic efficiency, and durability. A variety of portable electronics occupy a large portion of our daily lives and LIB is used as a power source for them. In recent years, LIB has also been used in the electric vehicles and large-scale ESS for industrial applications, thus the usage of LIBs will further increase in the future. With this trend, demand for LIB with high capacity, long cycle life, and high stability is rapidly increasing. Furthermore, ease of use and material abundance are being important consideration factors in battery development.³

LIB is mainly composed of the cathode, anode, separator, and electrolyte. Among them, cathode is the most important component determining energy density, cycle life, and battery price. This work introduces basic knowledge of a LiCoO_2 , the most well-known LIB cathode material with a layered structure, and addresses issues related to the high voltage operation focusing on the layered cathode materials.

a



b

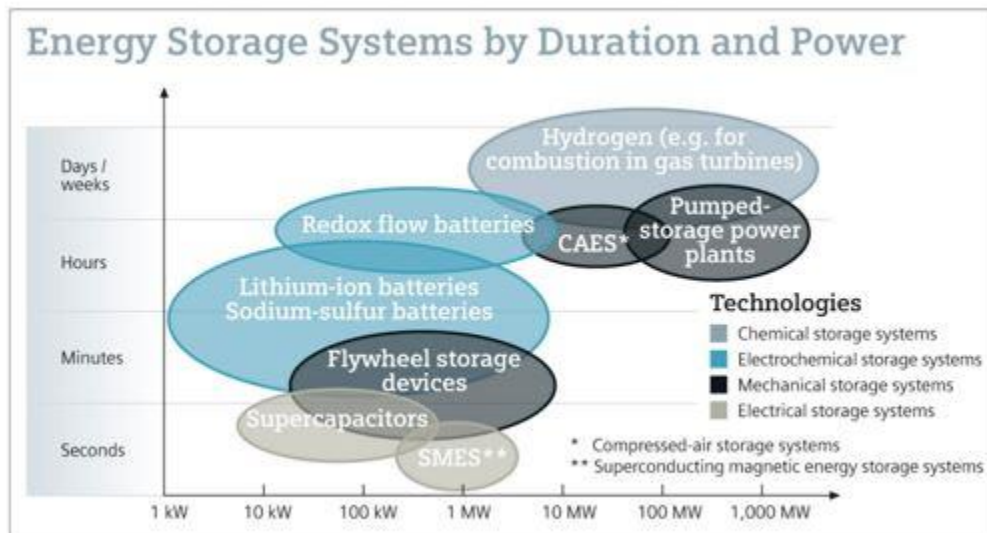


Figure 1. (a) Energy storage systems (ESSs) utilizing various energy sources.² (b) The duration and power of various ESSs.

1.1 Layered LiCoO₂ cathode material

To date, various cathode materials for LIBs with layered (LiMO₂, M= Co, Ni, Mn or its combinations), spinel (LiMnO₄), and olivine (LiMPO₄, M= Fe, Co, Mn) structure have been developed.⁴ Among them, layered LiCoO₂ (referred to as LCO) was commercialized for the first time. The LCO belongs to an α -NaFeO₂ crystal structure, which has an O-Li-O-Co-O-Li-O arrangement and the R-3m space group. In the LCO crystal structure, cobalt and lithium ions alternately occupy the octahedral site of the cubic closed packed oxygen atom array. (Figure 2). Li ions in this layered cathode material have 2-dimensional diffusion pathway along its slab.

The LCO has a high theoretical capacity of 274 mAh g⁻¹, but only ~60% of this capacity is available in commercial LIBs. This is because a cut-off voltage of the LCO cell is limited to 4.4 V (vs Li/Li⁺) and the active material undergoes severe degradation at higher voltages. Many researchers have revealed degradation mechanisms at high voltages, including phase transition from the hexagonal to a monoclinic phase,⁵⁻⁶ dissolution of Co ions,⁷⁻⁸ formation of the spinel or rock salt phase at the surface,⁹⁻¹⁰ and various side reactions with electrolytes.¹¹⁻¹² Notably, transition toward the monoclinic phase is irreversible, which results in only partially reversible intercalation and deintercalation of Li ions and eventually significant capacity fading.

Recently, increasing cost of cobalt source and ever-growing demand for LIBs with higher energy density have led to the replacement of the LCO with LiNi_xCo_yMn_zO₂ ($x + y + z = 1$) cathode materials. Nevertheless, the LCO is still one of the most attractive LIB cathode materials for portable electronics because of its large-scale synthetic capability, high electrode density (≥ 4.0 g cm⁻³), high redox potential (~ 4 V vs Li/Li⁺) with decent capacity as well as excellent stability against moisture.¹³ Accordingly, extensive research efforts to increase the energy density of the LCO have been made, resulting in higher cut-off voltage by modifying the surface and bulk properties. However, the practical specific capacity is still limited, necessitating other better breakthroughs.

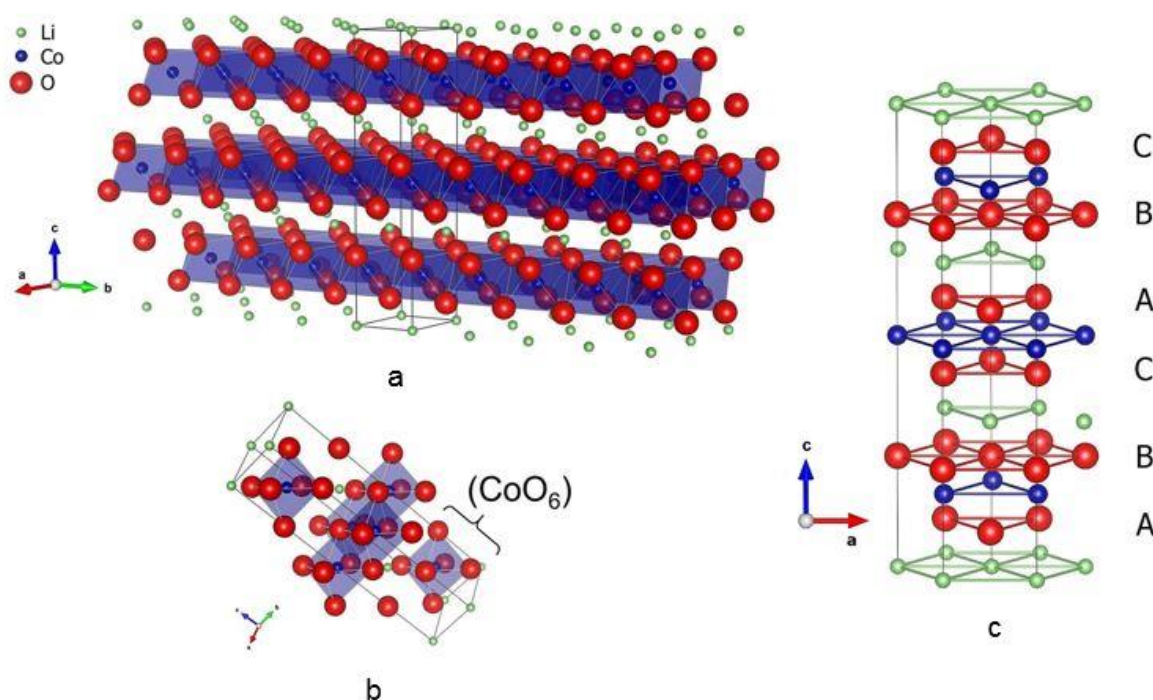


Figure 2. (a) Crystal structure of the LiCoO₂. (b) Octahedral CoO₆ structure. (c) ABCABC stacking arrangement of the LiCoO₂.¹⁴

1.2 High voltage operation of layered cathode materials

Increasing the cut-off voltage is one of the best approaches to enhance the energy density of the cathode materials. However, it is not feasible yet as the high voltage cycling induces severe deterioration in electrochemical performances of the cathode. One of the most well-known degradation mechanisms in high voltage environments is the continuous electrolyte decomposition at the cathode-electrolyte interphase.¹⁵ For the long-term operation of the cell, it should be charged and discharged within the electrochemical stability window of the electrolyte. In general, the electrochemical window of an electrolyte is determined by its highest occupied molecular orbital (HOMO) and lowest unoccupied molecular orbital (LUMO) energy level.¹⁶ Ideally, the redox potential of the cathode material should be lied above the HOMO energy and that of the anode should be lower than the LUMO energy level. However, the operating potential of most commercialized graphite anodes (~ 0.2 V vs. Li/Li⁺) lies beyond the LUMO energy level of conventional organic electrolytes, which gives rise to the inevitable anode-electrolyte reactions at the anode surface. Hence, the formation of a stable solid-electrolyte interphase (SEI) is highly important for the reversible cell operation (Figure 3).¹⁷⁻¹⁸

As for the cathode, the redox potential would be placed lower than the HOMO energy level of the

electrolyte when charged to higher voltages than conventional case, which results in the deviation from the electrochemical stability window. Accordingly, electrons can move from the cathode to the electrolyte, providing a thermodynamic driving force for the electrolyte decomposition. The cathode-electrolyte reactions cause not only a loss of the active material and Li ions, but also an increase in the internal resistance resulted from the accumulation of the side reaction products at the cathode-electrolyte interphase. In addition, extended Li extraction from the crystal structure of the cathode material leads to the irreversible structural change, and eventually severe capacity fading.¹⁹⁻²¹ Moreover, inactive cell components including the conductive carbon, separators, binders, and current collectors can be degraded at high voltage regions.¹⁶ This section will discuss degradation mechanisms of the layered cathode materials at high voltages and previous studies to resolve these problems.

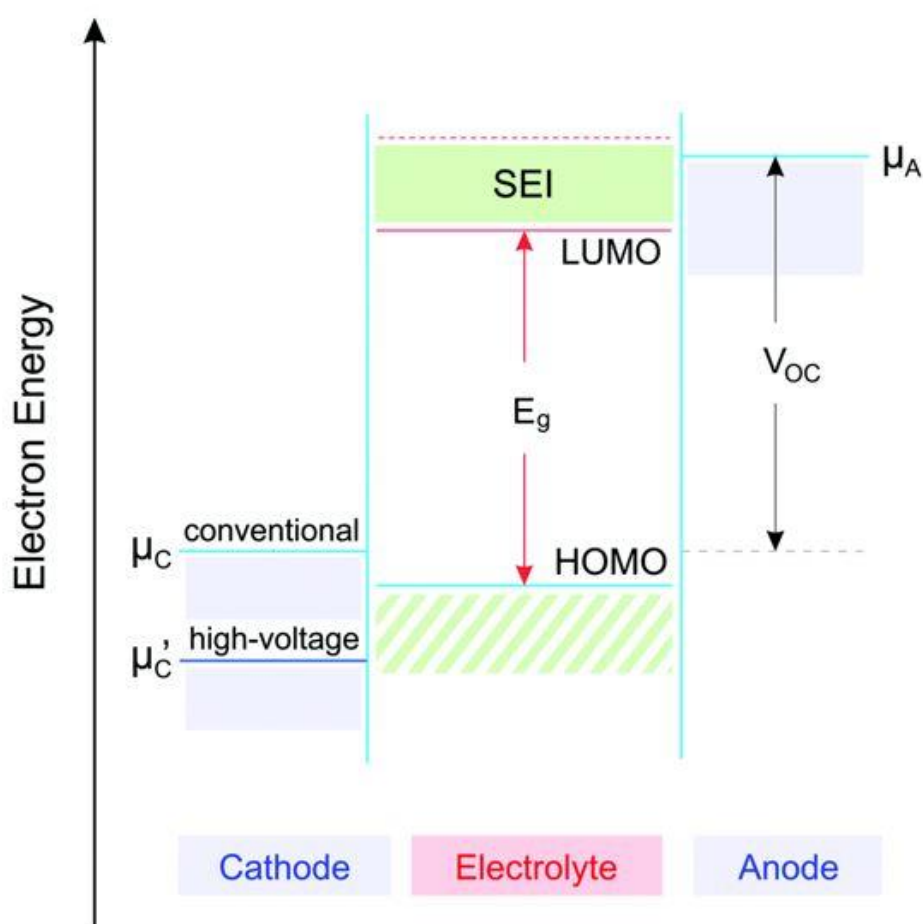


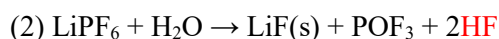
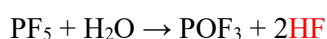
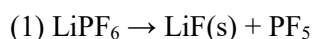
Figure 3. A scheme showing the electrochemical voltage window of an electrolyte.¹⁶

1.2.1 Degradation mechanisms of layered cathode materials in high voltage environment

Parasitic electrolyte decomposition on charged cathode surface

As mentioned above, the electrolyte becomes thermodynamically unstable at high voltages because of a change in the electrochemical potential of the cathode. Furthermore, nucleophilic surface oxygen in the highly delithiated cathode materials can attack the electrophilic carbonate solvent molecules of the electrolyte solution. For example, the ring opening reaction of the ethylene carbonate (EC) can arise at the cathode surface, forming Li_2CO_3 , semicarbonates, polycarbonates, Li alkoxides and other products (Figure 4b).^{16, 22} These organic and inorganic compounds increase an interphase resistance by accumulating on the cathode surface, which adversely affects the electrochemical performance of the cell. As a rule, a nucleophilicity of the surface oxygen in layered metal oxides becomes stronger with a greater electronegativity of the transition metal (TM) and a covalency between the TM and oxygen. Thus, it is generally accepted that decomposition of the EC solvent is more severe in Ni-based cathode materials than Co-based cathode materials (Figure 4a).

The breakdown of the electrolyte can be accelerated by acidic species originated from the hydrolysis of the LiPF_6 salts.²³



These unwanted side reactions not only continuously consume the extra Li ions but also contribute to the impedance growth on the electrode surface during cycling, which eventually leads to the deterioration in cell performances.²⁴

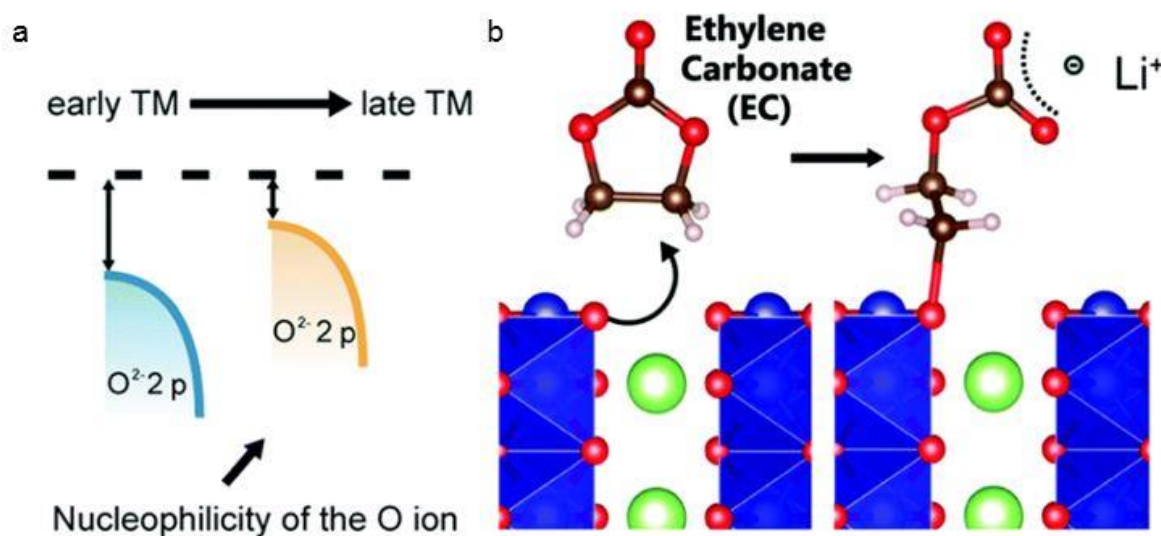


Figure 4. (a) Nucleophilicity of the oxygen at the delithiated cathode surface with the atomic number of transition metal. (b) Nucleophilic attack at the surface of layered oxide and EC decomposition.¹⁶

TM dissolution and chemical crossover between the cathode and anodes

Reduction and dissolution of the TM from the cathode surface have been generally accepted as one of the main degradation mechanisms of layered cathode materials at high voltages. TM ions should remain in the crystal lattice of the cathode material and participate in redox reactions during cycling. However, after the active materials contact with an electrolyte or after cycling, surface TM ions are partially reduced to the divalent state by the reactions with the electrolyte.²⁵⁻²⁷ This is an irreversible process, which results in the active material loss and an impedance buildup derived from the formation of the resistive layer at the cathode surface, and eventually capacity fading. In addition, some of TM ions are extracted from the cathode crystal structure and dissolved to the electrolyte. Dissolved TM ions and side reaction products at the cathode surface can migrate to the anode side by the concentration gradient or electric field force. They can be accumulated on the separator surface during this process, which hinders the facile transport of Li ions by clogging the separator pores and results in the internal resistance buildup.¹⁶ If the TM ions pass through the separator pores and reach the anode side, it can be deposited on the anode surface owing to the low potential of the negative electrode. This generally accompanies the decomposition of the extra electrolyte and formation of the unstable SEI layer.^{16, 28-30} This phenomenon is referred to as a chemical crossover, which causes a sluggish Li ion transport and localized Li plating as well as Li dendrite formation, eventually leading to the internal short circuit.

Some mechanisms to explain the TM dissolution and the crossover have been proposed, including the attack of acidic species to the cathode active materials and disproportionation reaction (e.g., $2Mn^{3+}$

$\rightarrow \text{Mn}^{2+} + \text{Mn}^{4+}$) within the cathode material.³¹⁻³² However, detailed mechanisms of the TM dissolution and chemical crossover between the cathode and anodes is still under debate.³⁰ These phenomena induce cell degradation in most layered cathode materials, especially in the manganese-based cathode materials, which has prompted an extensive research efforts. A recent study by Cho et al. reported that the Ni ion crossover from Ni-rich cathode with a Ni content of $\geq 80\%$ facilitates the formation of unstable SEI on the anode surface and cell degradation (Figure 5).³³ The dissolution of Co ions and Co ion crossover on the anode surface have also been reported in the LCO/graphite cell at a cut-off voltage of ≥ 4.2 V.^{7, 34} However, most previous reports provide only the evidence of Co deposition on the anode surface and the electrochemical cycling data, which cannot explain the connection between two phenomena clearly. They did not demonstrate that the Co ion crossover can affect the formation of unstable SEI layer or Li dendrite on the anode surface, which eventually deteriorate the anode capacity. In addition, other mechanisms such as crack formation or irreversible phase transition also should be considered. Indeed, as migrating species from the cathode is extremely complicated and cannot be detected quantitatively, their impacts on the anode SEI layer and electrochemical performances are still elusive. Therefore, it is essential to clearly reveal the major cause of the cell degradation in high voltage environments through the comprehensive analysis investigating both the surface and bulk properties as well as their connection to the electrochemical performance.

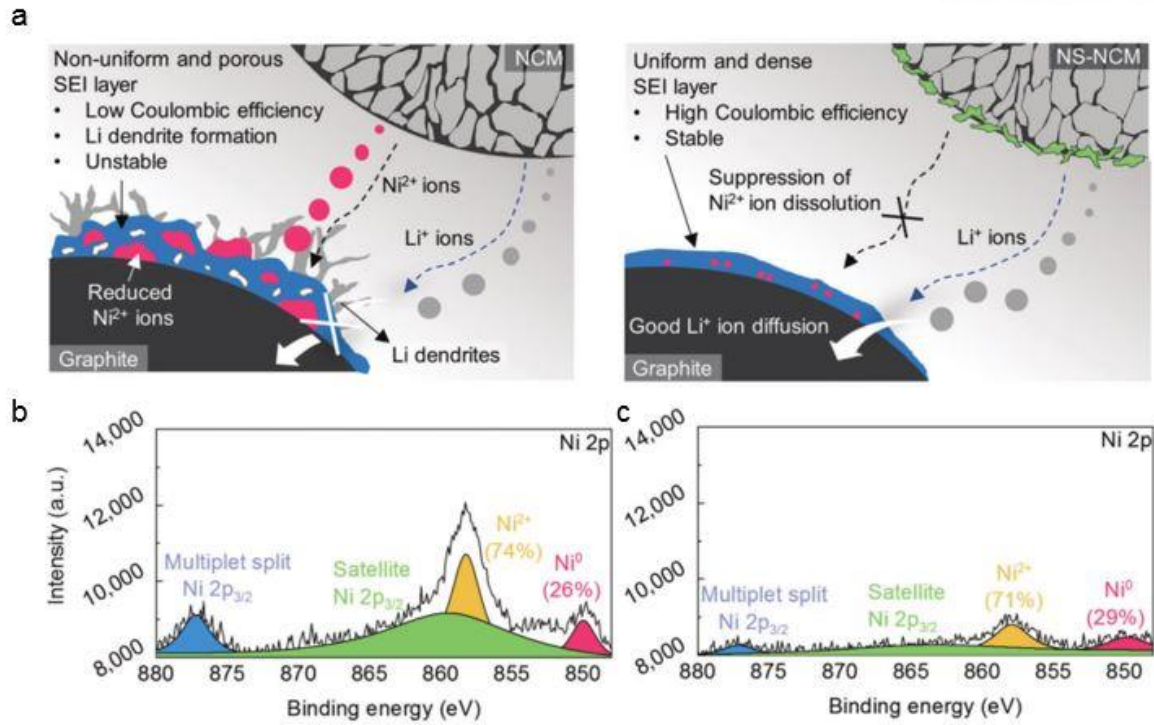
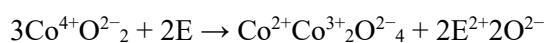


Figure 5. (a) Illustrations showing the effects of the nanostructured stabilizer which can suppress nickel ion dissolution of the NCM ($\text{LiNi}_{0.8}\text{Co}_{0.1}\text{Mn}_{0.1}$). Ni 2p X-ray photoelectron spectroscopy (XPS) spectra of the graphite anode in the (b) NCM/graphite full-cell and (c) NS-NCM/graphite full-cell after the cycling. Nanostructured stabilizer-incorporated NCM was denoted as NS-NCM. More Ni^{2+} ions were detected on the anode surface of the NCM/graphite full-cell.³³

Bulk and surface phase transition

LCO, the most well-known layered cathode material, experiences the bulk phase transitions from the O3 to H1-3 and O1 phases when charged to above 4.5 V.^{5, 35-36} As it accompanies a change in the atomic stacking of O-Co-O slab, the LCO structure can be damaged during repeated high voltage charging, resulting in drastic capacity fading (Figure 6).^{20, 36} Additionally, an atomic stacking change contributes to oxygen loss from the LCO crystal lattice and the evolution of the spinel phase at the LCO surface. During the high voltage charging process, most Co ions are oxidized to the tetravalent state (i.e., from $\text{Li}^+\text{Co}^{3+}\text{O}^{2-}_2$ to $\text{Co}^{4+}\text{O}^{2-}_2$), which can be easily reduced to the spinel-like Co_3O_4 phase through the reaction with the electrolyte at the cathode surface:



where E is the electrolyte which acts as a reducer.²⁰ This newly formed phase exhibits lower Li-ion

conductivity than the original layered phase, leading to the capacity fading.

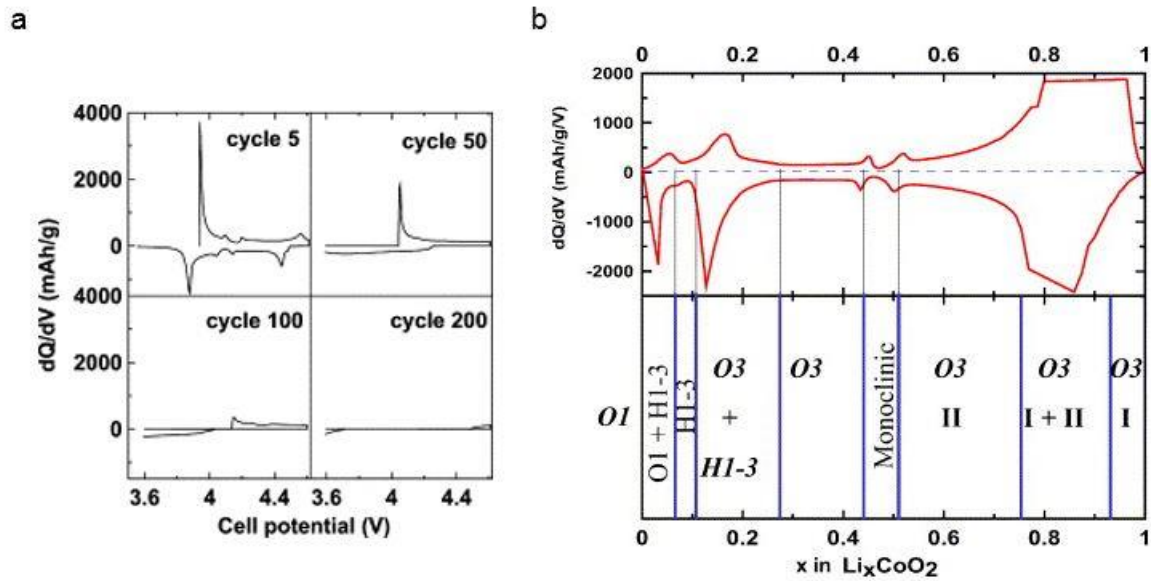


Figure 6. (a) Differential capacity vs. voltage curves of the LiCoO_2 (LCO) cell charged to 4.6 V for different cycles, which shows the irreversible phase transition of the LCO at high cut-off voltage. (b) Phase diagram of Li_xCoO_2 according to the Li contents ($0 < x < 1$).³⁶

In the Ni-based cathodes, it is well-known that the active material degradation is originated from the migration of TM ions into the Li slab (cation mixing), which leads to the evolution of the disordered phase near the surface region (Figure 7).³⁷⁻³⁹ It was directly observed using the atomic resolution scanning transmission electron microscopy (STEM) and electron energy loss spectroscopy (EELS) mapping analyses by Wang's group.³⁹ They revealed that the high voltage cycling creates oxygen vacancies, which facilitate the reduction of neighboring TM ions and consequent migration to the Li layers. They also revealed that Ni ions preferentially migrate to the Li slab rather than Co and Mn ions, inducing the structure disordering in the $\text{LiNi}_{1/3}\text{Co}_{1/3}\text{Mn}_{1/3}$ (NCM333). The possibility of Li vacancies would be larger near the surface than other regions because most Li ions are extracted from the surface. Hence, the cation migration and phase transition arises mainly at the surface.³⁸ A surface disordered phase functions as a passivation layer, which hinders the diffusion of Li ions and eventually reduces the cell capacity. Interestingly, the surface phase transition can occur just after the electrolyte exposure.³⁸

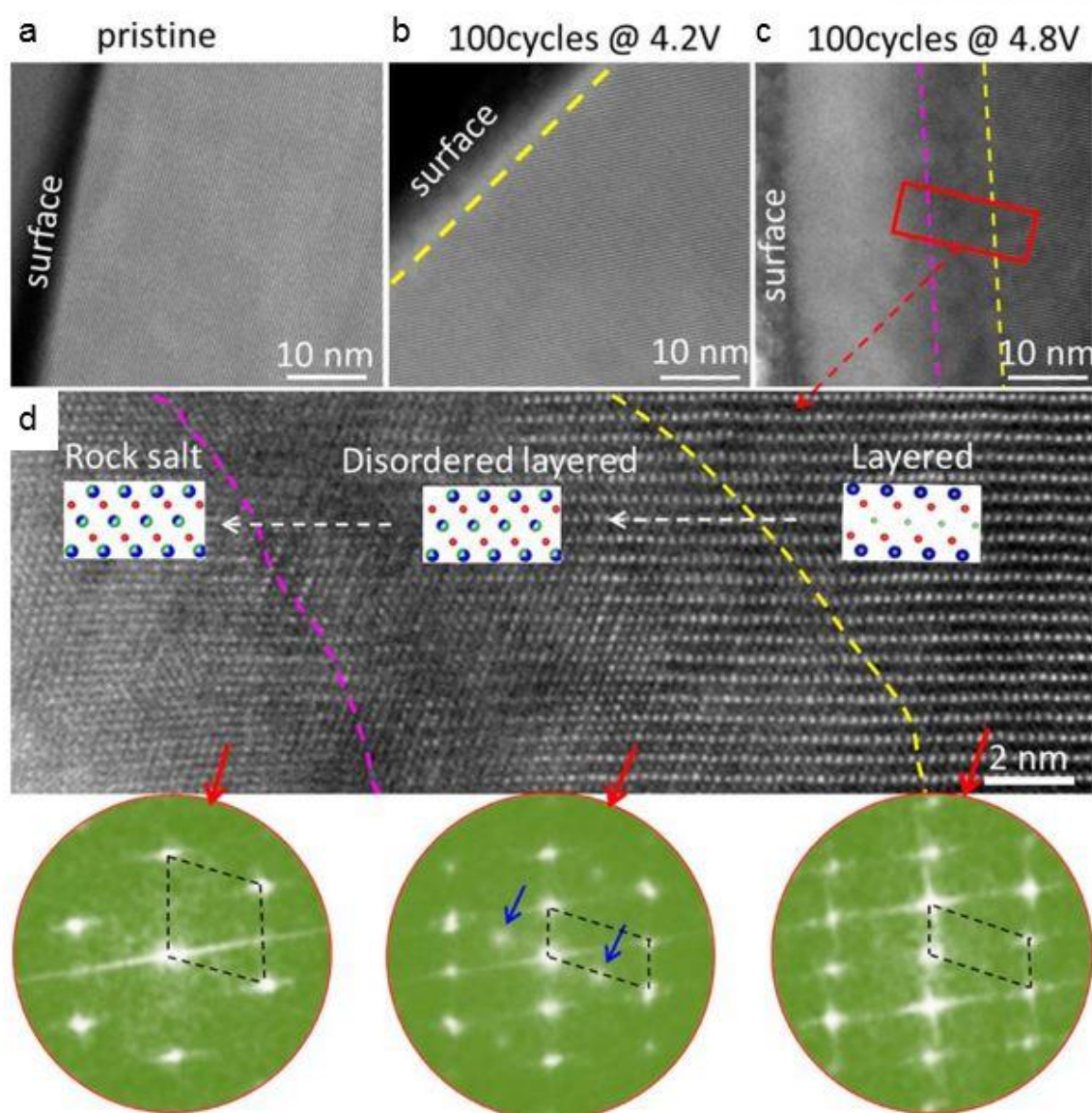


Figure 7. HADDF-STEM images of the NMC333 surface. (a) Pristine sample, (b) after 100 cycles with a cut-off voltage of 4.2 V, and (c) after 100 cycles with a high cut-off voltage of 4.8 V. (d) Magnified STEM image from the red box in (c). The insets are the models illustrating lattice change from the surface into the bulk, where transition metal, oxygen, and Li ions are denoted by blue, red, and green balls, respectively. The surface reconstruction layer was indicated by yellow dashed lines. Fast Fourier transformation (FFT) patterns from each region in (d) are shown, where blue arrows indicate migrated TM ions and dashed black frames show the unit cell of three different regions.³⁹

Intergranular/intragranular cracks

Recently, most state-of-the-art Ni-based cathode materials are synthesized through the co-precipitation method, constructing the secondary particles. In general, the intercalation and deintercalation processes in the layered cathode materials accompany the lattice expansion and shrinkage.⁴⁰ However, as each primary particle has different crystallographic orientation, it experiences an anisotropic volume change during cycling.⁴¹ Such continuous lattice volume change induces severe strain along the grain boundary, resulting in microcracks between primary particles. This type of cracking is termed as an intergranular crack, which has been well-known as one of the major degradation mechanisms of Ni-based cathode materials. The intergranular cracks cause the loss of connectivity between primary particles, leading to the poor electrical conductivity. Furthermore, when the newly created surface derived from the cracks is exposed to the electrolyte, it consumes the extra Li ions through the side reaction.⁴² Besides intergranular cracks, intragranular cracks have also been observed in harsh conditions such as high temperature, high voltage operation, and long-term cycling. These small cracks in the primary particle have been observed in layered cathode materials such as LCO,^{20, 43} NCM.^{42, 44-45} They can also create new surfaces that may be exposed to the electrolyte. More severely, the intragranular cracking is related to the structural degradation and mechanical failure of the active materials. According to the study from Wang's group,⁴² a degree of intragranular crack formation becomes greater at higher cut-off voltage (Figure 8a). They proposed that higher cut-off voltage causes deeper Li-ion extraction, which gives rise to a severe lattice change and internal strain within the particle, and eventually structural instability. The internal strain results in the splitting between two neighboring transition metal slabs and the formation of a dislocation. Generally, this dislocation propagates along the (003) plane and creates bigger cracks, which will deteriorate the cell capacity (Figure 8b). Another study from this group⁴⁵ revealed that thermally induced intragranular cracks have similar formation mechanisms with those of electrochemically induced, including the oxygen release and surface phase transformation (Figure 8c).

To summarize, the degradation process of layered cathode materials at high voltage is significantly complicated as it arises from not only the surface, but also the bulk structure. Accordingly, intensive research efforts to resolve these problems have been made over the past decade, which will be introduced in following part.

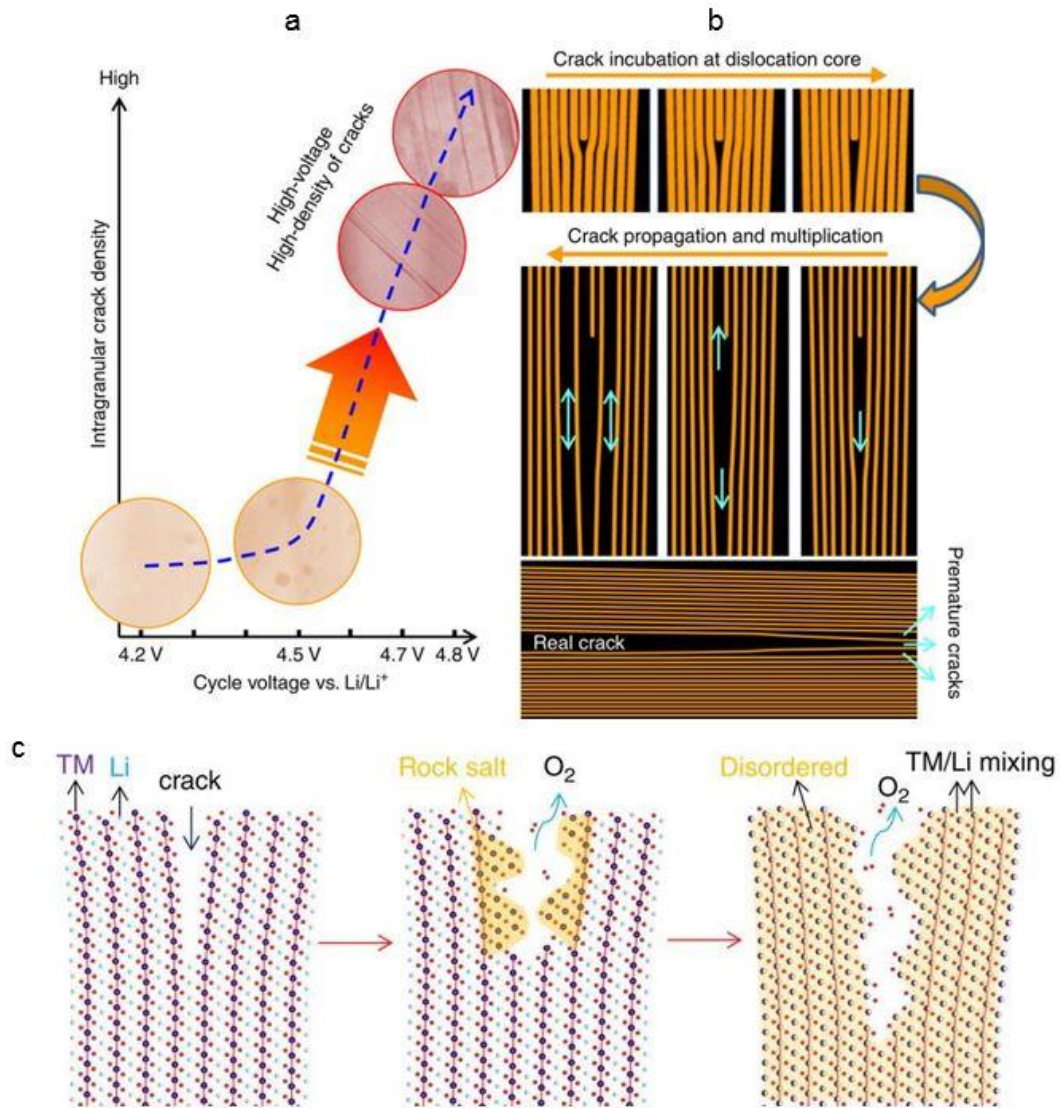


Figure 8. (a) A graph and high angle annual dark field (HAADF) images illustrating the relationship between the degree of intragranular cracks and cycling voltage. (b) Schemes for crack incubation and propagation process assisted by the dislocation.⁴² (c) A crack-propagation process, accompanying the oxygen loss and phase transformation.⁴⁵

1.2.2 Previous strategies for high voltage operation of layered cathode materials

Aforementioned problems of layered cathode materials at high voltage can be summarized as follows: 1) The structural instability of the cathode surface derived from side reactions with the electrolyte, 2) the intrinsic structural instability of the cathode active materials, 3) the electrochemical instability of the electrolyte. Previous research strategies to resolve these problems include the surface coating of inorganic materials, doping of heteroatom, and development of electrolyte additives.

For example, Cho et al. reported surface coating of metal oxides such as ZrO_2 , Al_2O_3 , which significantly improved the cycle retention of the LCO at high cut-off voltage (≥ 4.4 V).^{6, 46} The improvement was mainly attributed to the passivation effect of a coating layer against side reactions, which can suppress the impedance growth of a cell during cycling.³⁶ In addition, other various modifications including post-heat treatment, metal-phosphate and polymer coating were reported.^{12, 15, 20, 36, 47-49} For instance, Dahn's group revealed that post-heat treatment without any coating precursor can improve the surface stability of the LCO by eliminating the residual Li and water species within the cell.³⁶ Another study from Lee et al. unveiled that post-heat treatment creates a spinel- $\text{Li}_x\text{Co}_2\text{O}_4$ phase on the LCO surface, which prevents side reactions and functions as a conductive layer.⁴⁸ Among a variety of surface coating methods, AlPO_4 coating on the LCO exhibited a remarkable improvement in cycle performance at high voltages. The enhanced cycling stability was originated from the formation of Li-conductive Li_3PO_4 and $\text{LiAl}_x\text{Co}_{1-x}\text{O}_2$ phases, which can suppress the Co dissolution and buildup of charge transfer resistance during cycling (Figure 9).⁴⁷ To combine the coating effects of various elements, some binary hybrid materials were proposed as coating precursors. For example, spinel- MgAl_2O_4 modification on the LCO was reported, which can form the $\text{LiAl}_x\text{Co}_{1-x}\text{O}_2$, $\text{LiMg}_x\text{Co}_{1-x}\text{O}_2$ phase and their combinations at the surface region.⁴⁹ Mg^{2+} ions contributed to the improved conductivity and Al^{3+} ions could stabilize the layered structure of the LCO by forming the solid solution. As a result, this strategy showed combined coating effects of Al_2O_3 and MgO modifications, which significantly improved the cycle retention and rate capability of the LCO.

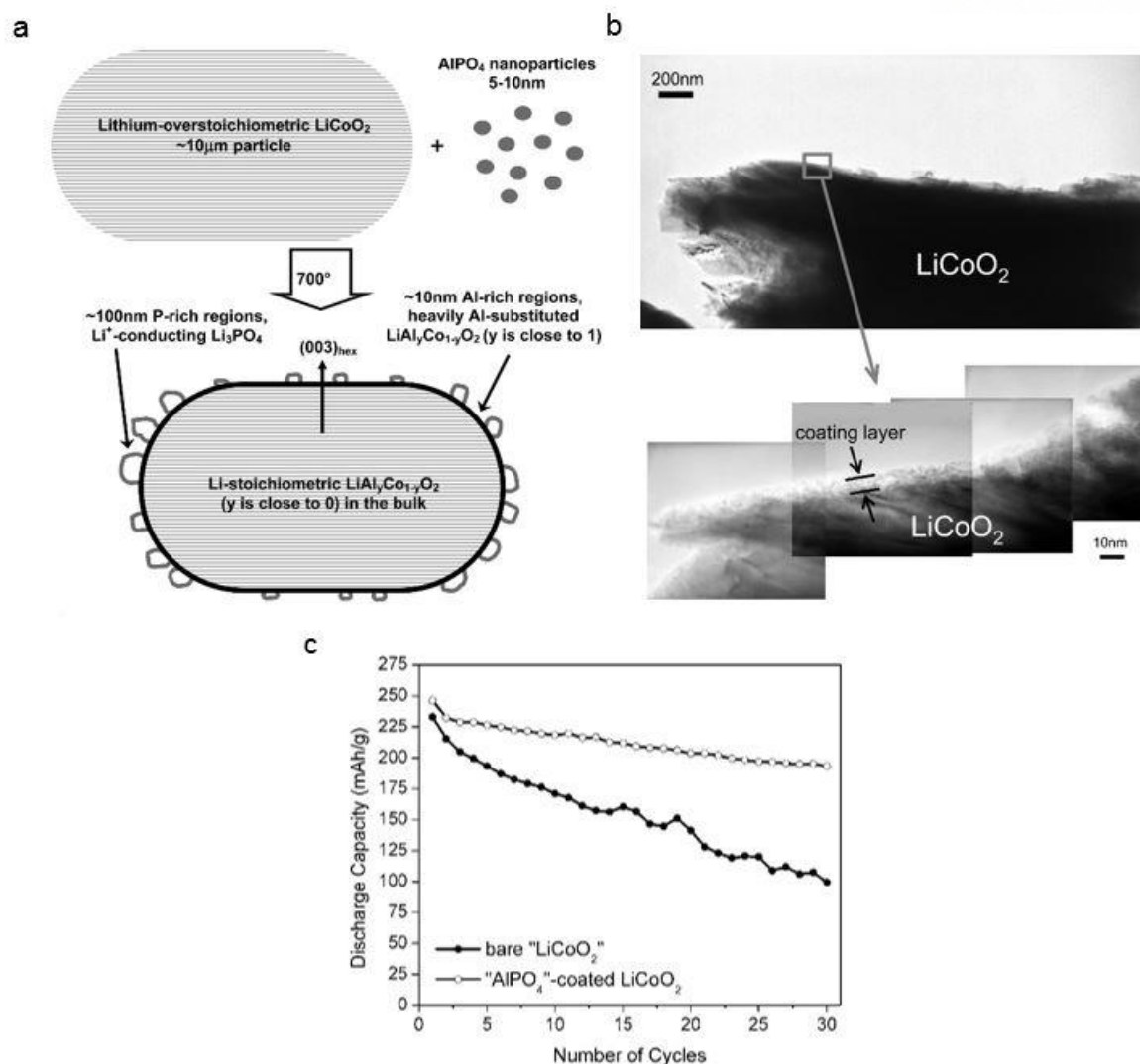


Figure 9. (a) A schematic showing the mechanism of AlPO₄ coating on the LiCoO₂ cathode material, resulting structure and composition. (b) Surface TEM images of the “AlPO₄”-coated LiCoO₂. (c) Electrochemical performance of the bare LiCoO₂ and “AlPO₄”-coated LiCoO₂ for 30 cycles. Voltage ranged from 3.0 to 4.7 V and charge/discharge C rate was C/5, except for the first cycle (C/10).⁴⁷

Meanwhile, extensive research attempts have been adopted to enhance the intrinsic structural stability of the cathode material through a doping of foreign metal elements such as Mg, Al etc.⁵⁰⁻⁵² It could improve the cycle retention of the LCO, whereas resulted in the lower initial capacity. Hence, minimum amounts of doping precursors were utilized for a practical use and generally post-surface modification was accompanied. Recently, Cho et al. reported a Ni doping on the LCO cathode materials. They noted that the different structural degradation mechanisms between the LCO and Ni-rich cathode materials are associated with their electrochemical reversibility.⁵³ In the LCO, an irreversible bulk-phase transition from the O3 to O1 phase is caused by the increased Coulombic repulsion between neighboring oxygen slabs at highly delithiated state. In the Ni-rich cathode materials, however, the migration of Ni ions to the Li slab results in the localized phase transformation at the cathode surface. They believed that the great electrochemical reversibility of the Ni-rich materials is attributed to the screen effect of migrated TM ions in the Li site. They adopted this concept to the LCO, which can delay the phase transition and thus results in the extended electrochemical reversibility. This hypothesis was validated by the in-situ XRD and HAADF-STEM analyses, and Ni-doped LCO showed improved cycle retention at the cutoff voltage of 4.5 V (Figure 10).

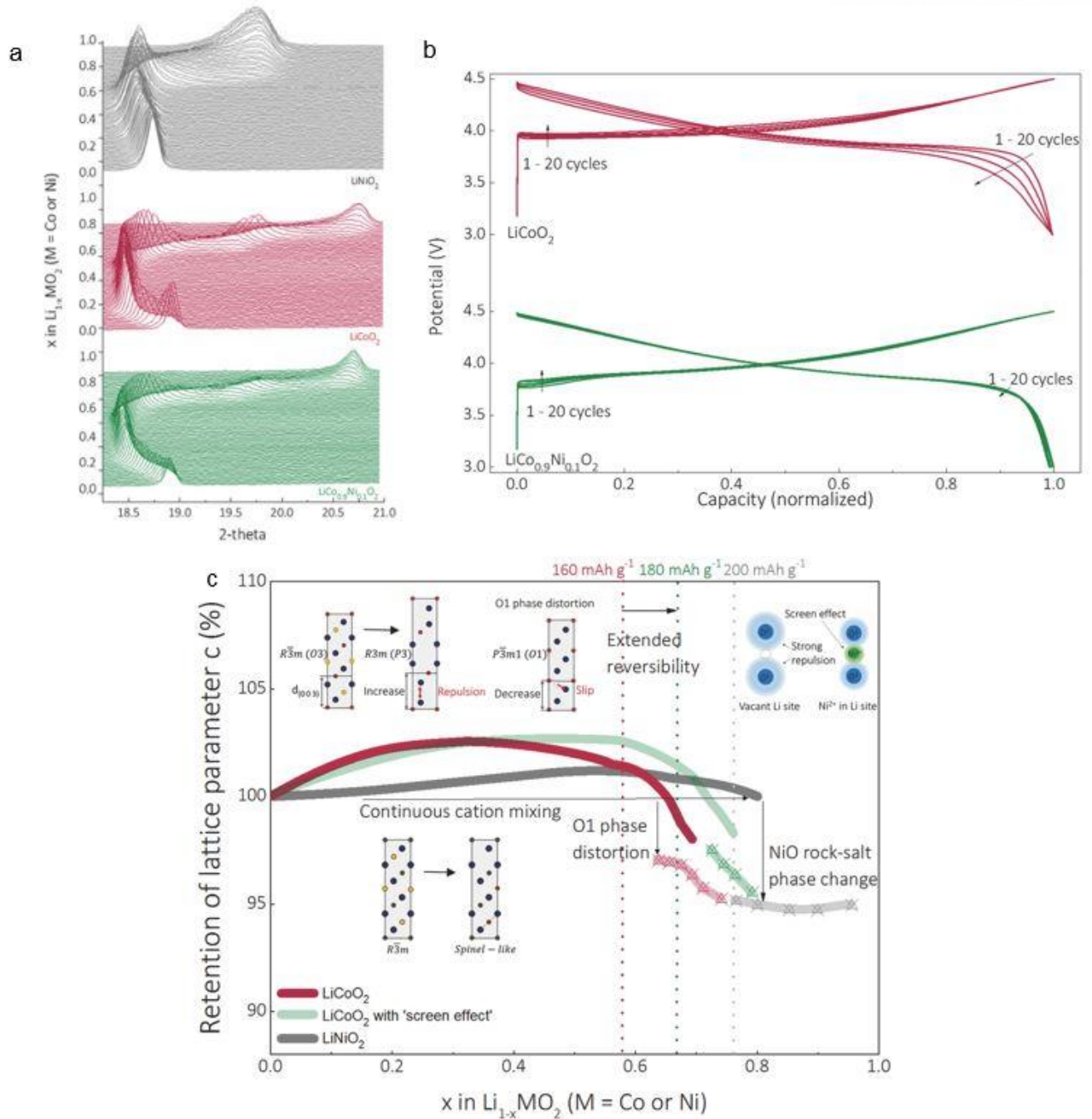


Figure 10. (a) In-situ XRD results of the LiNiO_2 , LiCoO_2 , and $\text{LiCo}_{0.9}\text{Ni}_{0.1}\text{O}_2$ (black, red, and green pattern, respectively) during charging process. (b) Voltage profiles of the LiCoO_2 and $\text{LiCo}_{0.9}\text{Ni}_{0.1}\text{O}_2$ during 20 cycles between 3.0 and 4.5 V. (c) A scheme showing phase transition and change in lattice parameter c during charging process.⁵³

In recent years, doping methods using foreign elements such as boron, zirconium, and vanadium has been adopted to the Ni-rich materials.⁵⁴⁻⁵⁶ For instance, Sun's group incorporated the excess Zr ions into the LiNiO_2 (denoted as LNO) during the co-precipitation process.⁵⁶ Zr-doped LNO showed relatively reversible $\text{H}_2 \leftrightarrow \text{H}_3$ phase transition than that of the pristine LNO, which was evidenced by $dq \, dV^{-1}$ and X-ray diffraction (XRD) analyses. This resulted in the improved cycle retention at cut-off voltage of 4.3 V. As more than 80% of Li ions are extracted from the LNO when charged to 4.3 V, the enhancement in structural stability through the doping methods appears to be necessary for the high-voltage operation of high-Ni content cathode materials.

As mentioned above, the electrolyte containing carbonate solvents is inevitably decomposed at the high voltages, deteriorating electrochemical performances of the cell. Thus, the development of functional additives that can stabilize the electrode surface is essential for the high voltage operation (≥ 4.5 V). For example, vinylene carbonate (VC) is well known as one of the most effective additives at the commercial stage. Dahn's group systemically identified the effectiveness of the VC in the Ni-based cathode material/graphite full-cell by comparing with other various functional additives.⁵⁷⁻⁵⁸ Fluoroethylene carbonate (FEC), lithium bis(oxalato)borate (LiBOB), and vinyl ethylene carbonate (VEC) also have been developed as other promising functional additives.¹⁶ These additives are generally decomposed during the charging process and produce stable interphases on both electrode surfaces, which protect the surface against deleterious side reactions.

1.2.3 Objective of this work

In this work, we report a high temperature solid-state surface modification as one of the promising approaches. The effectiveness of this simple and cost-efficient method was demonstrated using the large-sized LCO (D50 = $\sim 20\ \mu\text{m}$) as a cathode material. Each component of the LCO/graphite full-cell was thoroughly analyzed to find the major degradation mechanism in the high voltage environment. We found that the deterioration of layered cathode materials at high voltages was mainly attributed to the severe crack formation and structural collapse. Interestingly, Co ion crossover did not affect to capacity fading of the LCO/graphite full-cell, which is not consistent with earlier findings. During the high temperature calcination process, Mg ions diffused into the outermost and inner surface regions, forming the $\text{LiCo}_x\text{Mg}_{1-x}\text{O}_2$ phase. This robust phase protects the LCO surface against the Co ion dissolution and oxygen evolution, suppressing the bulk phase transition and crack formation. This led to the significant improvement in the electrochemical performances of the LCO in the extended voltage window (from 3.0 to 4.5 V vs. Li/Li^+). Especially in the full-cell system (voltage range: 2.7-4.4 V), modified-LCO/graphite cell exhibited excellent capacity retention of $\sim 87\%$ after 500 cycles, demonstrating the commercial viability of our approach. This finding could provide a new way for the commercialization of high-voltage layered cathode materials.

II. Experimental detail

Materials preparation

A pristine LiCoO_2 (LCO) was provided by LG Chem, Ltd. and used without any further modification. For the synthesis of coating precursor (magnesium phosphate), magnesium acetate ($\text{Mg}(\text{CH}_3\text{COO})_2 \cdot 4\text{H}_2\text{O}$, 4.952g) was dissolved in the ethanol (150 ml). And then phosphoric acid (H_3PO_4 , 85 wt%, 1.043 ml) diluted with ethanol (~ 10 ml) was slowly added into the solution, which results in the precipitation between Mg^{2+} and PO_4^{3-} . The solution was stirred at 350 r.p.m for 1 h, filtered and dried at 120 °C for 1 h. To prepare the magnesium phosphate-incorporated LiCoO_2 (M-LCO), the as-prepared coating precursor (0.171 g) was mixed with LCO powder (20 g) by a mechanical mixer at 2000 r.p.m for 3 min. The mixed powder was annealed at 900 °C for 5 h (heating rate of 5 °C min^{-1}) under the ambient air.

Cell fabrication and electrochemical measurements

All the electrochemical measurements were carried out using 2032R coin type half-cell and pouch type full-cell. To prepare the cathode composite electrode, cathode active material (96 wt.%) was mixed with Super-P (2 wt.%) and poly(vinylidene fluoride) binder (2 wt.%), dissolved in N-methyl-2-pyrrolidone (NMP). The resulting slurry was cast onto aluminum foil and then dried at 120 °C for 1 h. The mass loading level and electrode density of the cathode electrode were 15.2 mg cm^{-2} and 3.8 g cm^{-3} , respectively. This cathode electrode was assembled into coin type half-cells in Ar-filled glove box. Li metal was used as a negative electrode and 1 M LiPF_6 in ethylene carbonate (EC), dimethyl carbonate (DMC), and diethyl carbonate (DEC) (1:2:1, v/v/v) with 2 wt.% of vinylene carbonate as an additive (Panax Etec.) was used for an electrolyte. The assembled cells were evaluated with constant charge/discharge C rate of 0.1C for the first cycle (formation cycle) and 0.5/1.0C for the following (50) cycles between 3.0 V and 4.5 V (vs. Li/Li^+). For the rate capability test, the cells were cycled with a 0.2C charge C rate and different discharge rates of 0.2/0.5/1.0/2.0/3.0/5.0C. All the EIS data was obtained from Biologic VMP-300 potentiostat with frequency range from 1 MHz to 10 MHz and a DC voltage amplitude of 10 mV after fully charged to 4.5 V. The galvanostatic intermittent titration technique (GITT) was employed using coin type half-cells, cycled in the voltage range of 3.0-4.5 V at constant charge and discharge C rate of 0.5C for 8 min with a rest time of 1 h.

For the full-cell test, the anode composite electrode was prepared by blending artificial graphite (96 wt.%), Super-P (1 wt.%), carboxymethyl cellulose (CMC, 1.5 wt.%), and styrene-butadiene rubber (SBR, 1.5 wt.%). The mixed slurry was coated onto copper foil with a mass loading level of 6.8 mg cm^{-2} and dried at 80 °C for 1 h. The electrode was pressed to 1.5 g cm^{-3} , and then dried again in the

vacuum oven at 150 °C for 6 h. The loading level and electrode density of the full-cell cathode electrode were adjusted to 13.60 mg cm⁻² and 3.6 g cm⁻³, respectively. The same electrolyte with the cathode half-cell was employed in the full-cell test. The N/P ratio of the full-cell was ~1.12, and the cells were cycled between 2.7 and 4.4 V with charge and discharge C rate of 0.1C for the first cycle and 1C for the following (500) cycles. A degassing process was included during first charging.

Material characterization

To investigate the crystallographic structure of the cathode materials, the X-ray diffraction (XRD) patterns were obtained using Rigaku D/MAX 2500 V/PC X-ray diffractometer with Cu-K α radiation. A scan range was from 10° to 80° (2 theta) with a scan step of 0.02° and a counting time of 5 s. The morphology of the cathode active materials was observed by scanning electron microscopy (SEM, Verios 460, FEI). To examine surface chemistry and microstructure, the cross-sectioned cathode and anode particles were prepared by ion milling system (Model 1040 Nanomill, Fischione), and then analyzed using the SEM-attached energy dispersive X-ray spectroscopy (EDX, XFlash 6130, Bruker). The atomic-scale structural and elemental analysis was performed by a high resolution-transmission electron microscopy (HR-TEM, ARM300, JEOL) at 300 kV. Dual-beam focused ion beam (FIB, Helios 450HP, FEI) was utilized for TEM sampling. STEM-EDX result was obtained from HR-TEM attached EDX(Aztec, Oxford). To measure the amount of Co dissolution, the coin type half-cells were fabricated with Li metal anode, and firstly charged to 4.5 V. Then, the cells were disassembled in a glove box and the cathode materials were stored in the electrolyte at 60 °C for 4 weeks. After 1st, 2nd, and 4th week, the amount of Co ions in the electrolyte was investigated using the inductively coupled plasma (ICP). The same amount of cathode materials (69.4mg) and the electrolyte (10ml) were used for the test.

III. Results and discussion

3.1 Morphology, structure, and surface composition

Figure 11 shows SEM images of the pristine LCO (referred to as LCO) and modified LCO (referred to as M-LCO). Both LCO and M-LCO have almost same morphology and particle size (10~25 μm), which implies that our solid-state surface modification with a high temperature of 900 $^{\circ}\text{C}$ did not affect the morphology and particle size of the LCO. Meanwhile, some stuff could be found on the LCO surface, whereas the M-LCO had a relatively clean and smooth surface. It is believed that some remained Li ions on the surface diffused into the LCO lattice during the high-temperature sintering process, as the amount of residual Li decreased after the modification (Table 1). The XRD patterns of the LCO and M-LCO showed a typical layered structure with a space group of R-3m (Figure 12). Any significant changes in XRD peaks were not observed after the modification, indicating that our modification process hardly affects the lattice structure of the LCO.

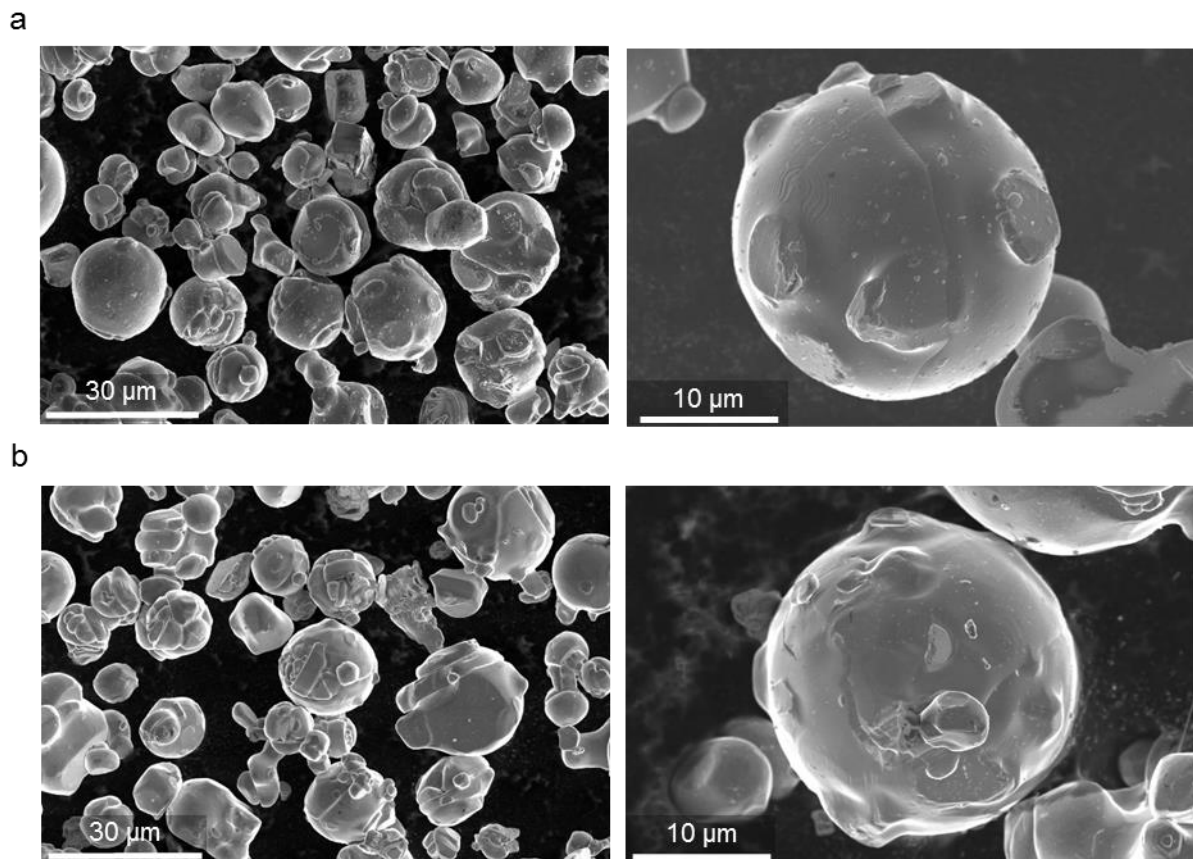


Figure 11. SEM images of the (a) LCO and (b) M-LCO.

Table 1. Physical properties of the LCO and M-LCO.

Physical property	LCO	M-LCO
Residual Li ($\text{Li}_2\text{CO}_3 + \text{LiOH}$) [ppm]	1150	< 500
Particle size (D50) [μm]	19.95	19.58

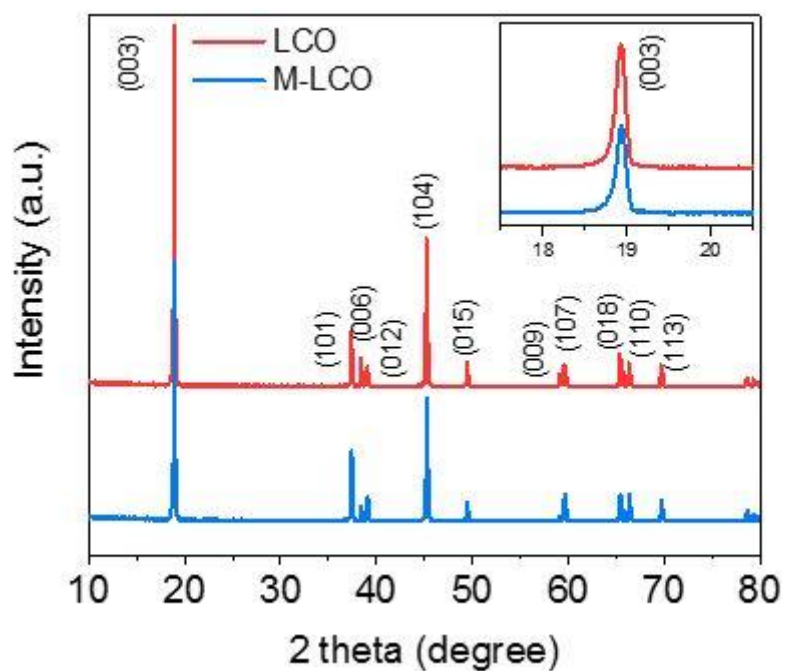


Figure 12. Powder XRD patterns of the LCO and M-LCO.

Next, the TEM and EDX analyses were carried out to investigate the effects of the modification on the LCO surface. As shown in Figure 13, Mg and P ions appeared to diffuse into the LCO surface. The incorporated Mg ions were mainly located at the surface with a thickness of over 100nm. The magnesium phosphate precursor would melt during the high temperature calcination process and the molten ions can diffuse into the LCO surface rather than create a coating layer on the surface. Interestingly, magnesium ions exhibited a concentration gradient from the surface to the subsurface regions (Figure 14, 15a). However, much smaller amount of phosphorus ions than magnesium ions were doped into the LCO surface, without having a concentration gradient. Most of undoped phosphorus ions were agglomerated on the LCO surface, creating phosphate compounds ($-\text{PO}_4$) without uniformity (Figure 15b). It would be difficult for phosphorus ion which favors the pentavalent state to substitute Co^{3+} , Li^+ , or O^{2-} ions. Therefore, it could be expected that P ions would not affect the electrochemical performance of the LCO, which will be proved through the electrochemical test in the following part. Figure 16a and b show the STEM images of the LCO and M-LCO surface, respectively. Both the surface and bulk structure of the LCO has layered structure with a space group of R-3m, while the outermost surface of the M-LCO changed into the rock salt phase during the high temperature calcination process. However, the modified M-LCO sample appeared to have overall layered structure in the fast Fourier transform (FFT) pattern, as the surface rock salt phase was very thin (≤ 2 nm).

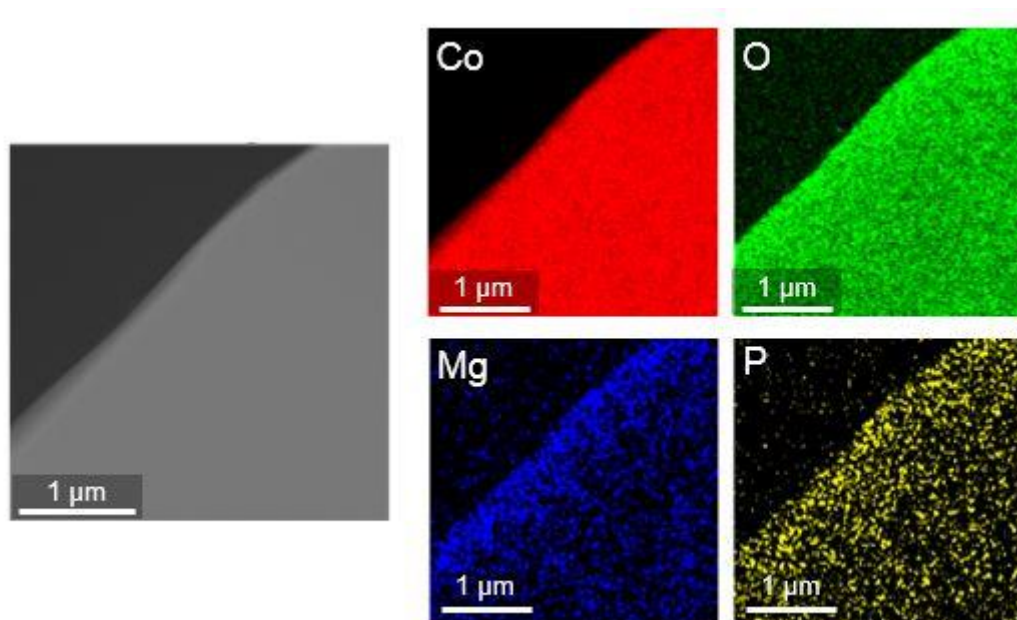


Figure 13. A scanning transmission electron microscopy (STEM) image and EDX mapping data of the M-LCO surface.

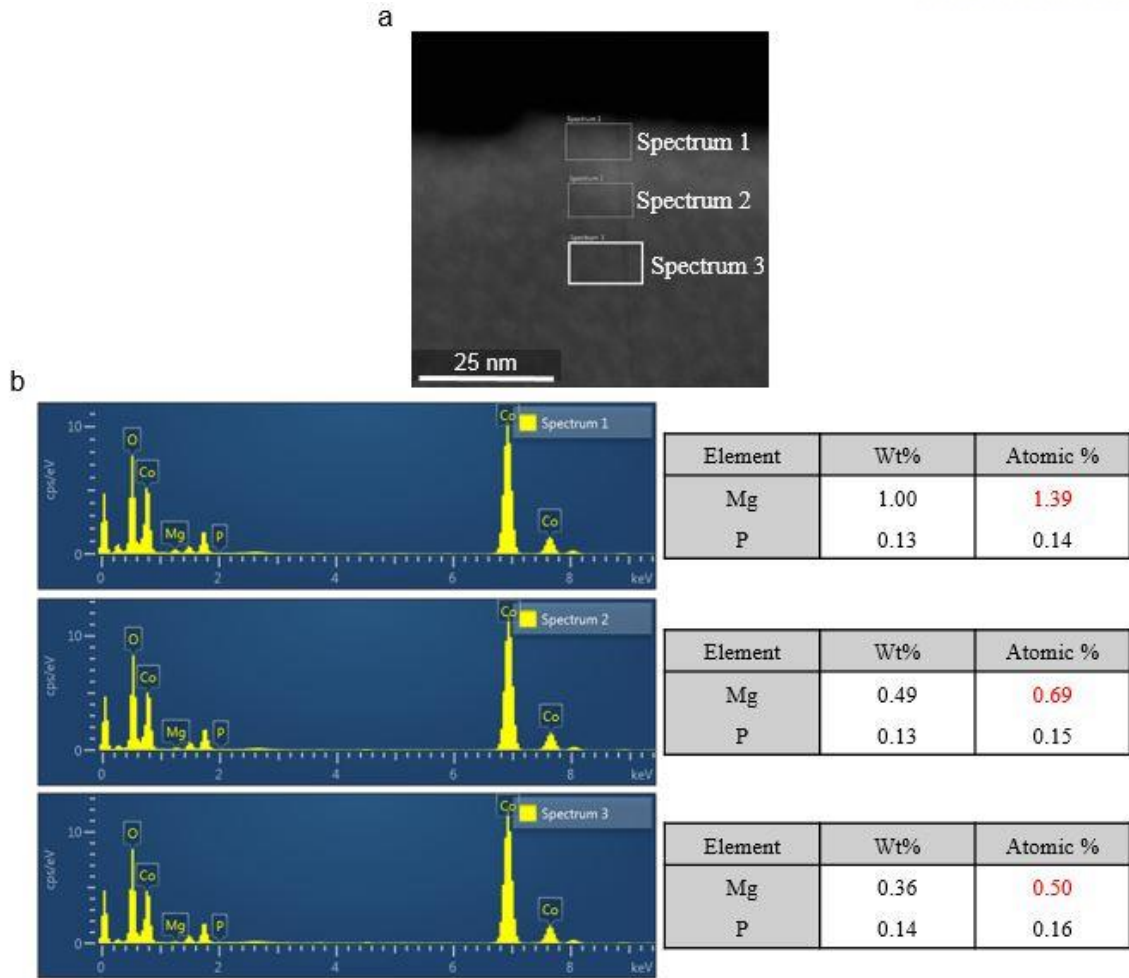


Figure 14. (a) A high angle annual dark field (HAADF)-STEM image of the M-LCO surface and (b) corresponding EDX spectrum results of each region in (a).

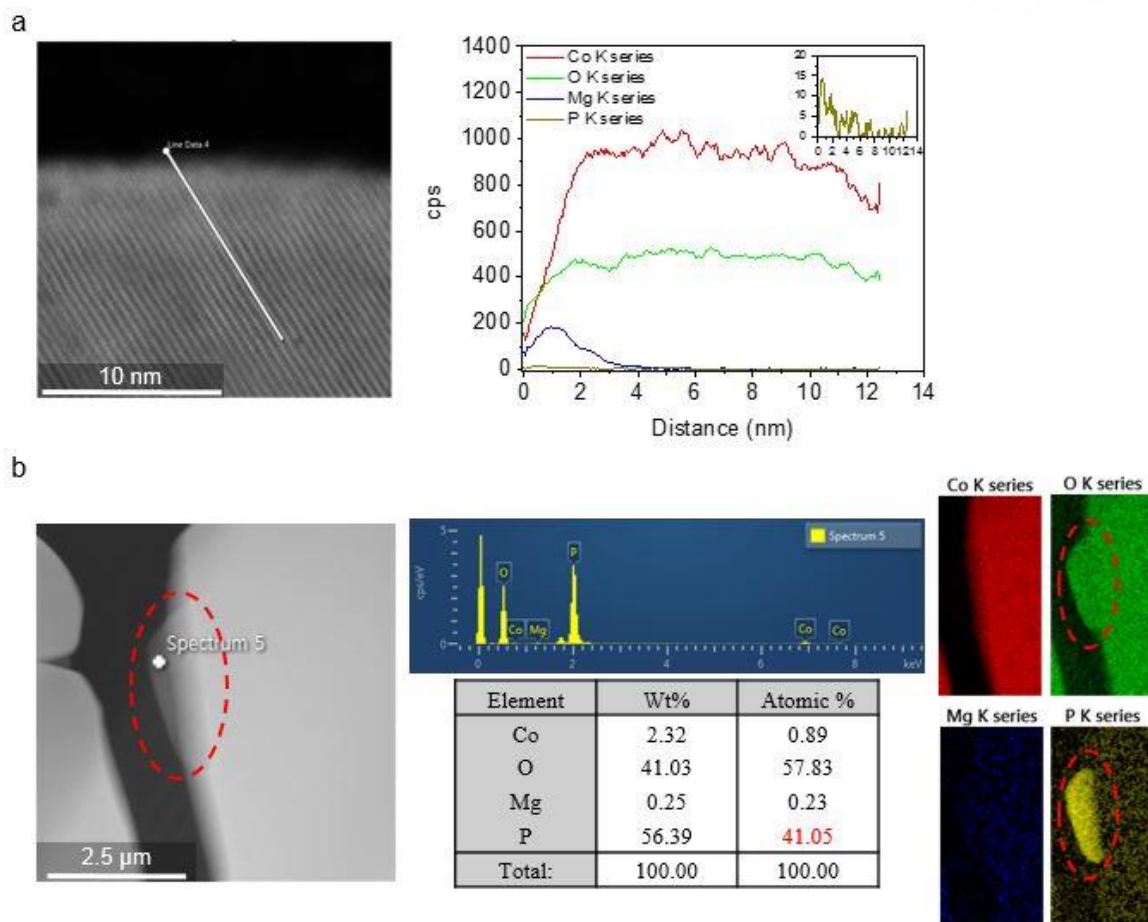


Figure 15. (a) A magnified STEM image and EDX line scanning of the M-LCO surface. The inset is the signal of P K series. (b) EDX point scanning from white dot region and mapping data, indicating agglomerating of P at the surface.

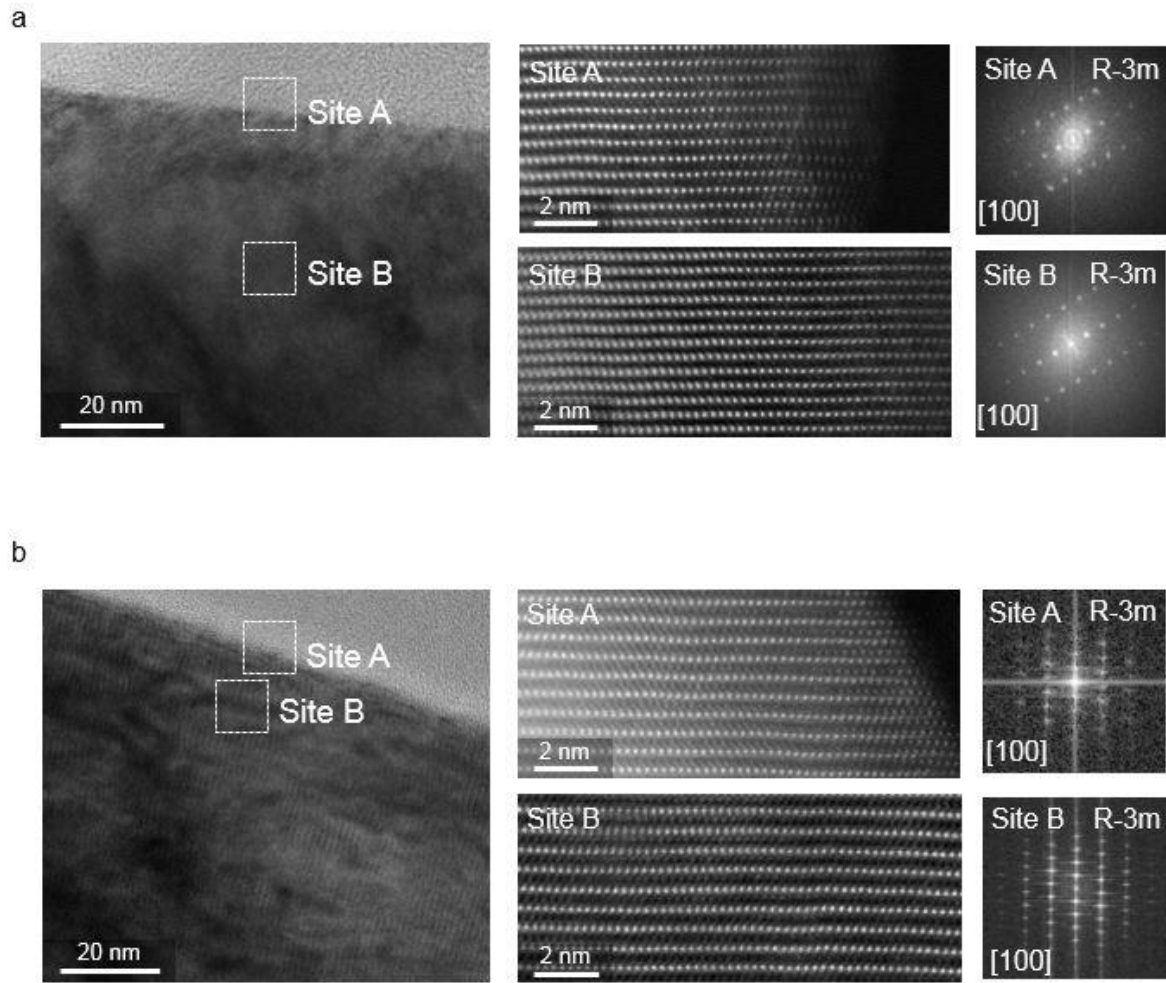


Figure 16. A magnified HR-TEM images of the (a) LCO and (b) M-LCO. Magnified STEM images of the outer (site A) and inner (site B) surface and corresponding FFT patterns are also shown.

3.2 Electrochemical results

The electrochemical performance of each cathode material was evaluated using a half-cell with a voltage range of 3.0–4.5 V. The LCO and M-LCO showed almost same reversible capacity of ~ 190 mAh g⁻¹ and Coulombic efficiency of $\sim 98\%$ in the formation cycle, as shown in Figure 17a. The room temperature cycle test was carried out just after the formation cycle with a charge and discharge C rate of 0.5 and 1.0C, respectively. As shown in Figure 17b, the capacity retention of the LCO cathode was significantly improved with the introduction of magnesium ions. After 50 cycles, the M-LCO retained 97.4% of its initial discharge capacity, whereas the LCO maintained only 72.4%. (Figure 17b). Additionally, we prepared other two modified LCO samples, which were then cycled under the same condition. One is a LCO sample doped with only magnesium ions using the Mg(OH)₂ precursor (equal moles of the Mg ions with the M-LCO were used), and the other sample is a post-heat treated LCO without any coating precursor. Two samples were denoted as MO-LCO and H-LCO, respectively. Interestingly, the MO-LCO showed excellent capacity retention after 50 cycles, which is nearly equal to the M-LCO (Figure 17b). Hence, it was validated that the P ions do not affect the electrochemical performance of the LCO, as most of the phosphorus agglomerates on the LCO surface and hardly diffuse into the LCO lattice. Meanwhile, Dahn's group revealed that the improved capacity retention of the metal oxide-coated LCO was mainly due to the heating process.³⁶ However, only 78.9% of the initial discharge capacity was maintained for the H-LCO after 50 cycles, which is 18.5% lower than the capacity retention of the M-LCO. The high temperature cycle test was also conducted at 60 °C. In the formation cycle, the LCO and M-LCO showed the high reversible capacity of 197 and 194 mAh g⁻¹ with Coulombic efficiency of 98.7 and 99.9%, respectively (Figure 17c). Surprisingly, M-LCO exhibits an excellent capacity retention of 96.6% after 50 cycles even at the elevated temperature, which is $\sim 40\%$ higher than that of the LCO (Figure 17d). The phase stability of the M-LCO was verified by dq/dV^{-1} curve (Figure 18). In general, the LCO has two peaks at about 4.1 and 4.2 V, which are related to the bulk phase transformation between two hexagonal (O3) phases.⁵⁹ However, these peaks disappeared even after the formation cycle and overall peak intensities decrease rapidly as cycling continues for the LCO, whereas the corresponding peaks for the M-LCO exhibit no significant change during cycling. This demonstrates that the introduction of the magnesium ions into the LCO surface could significantly improve the phase reversibility of the bulk structure.

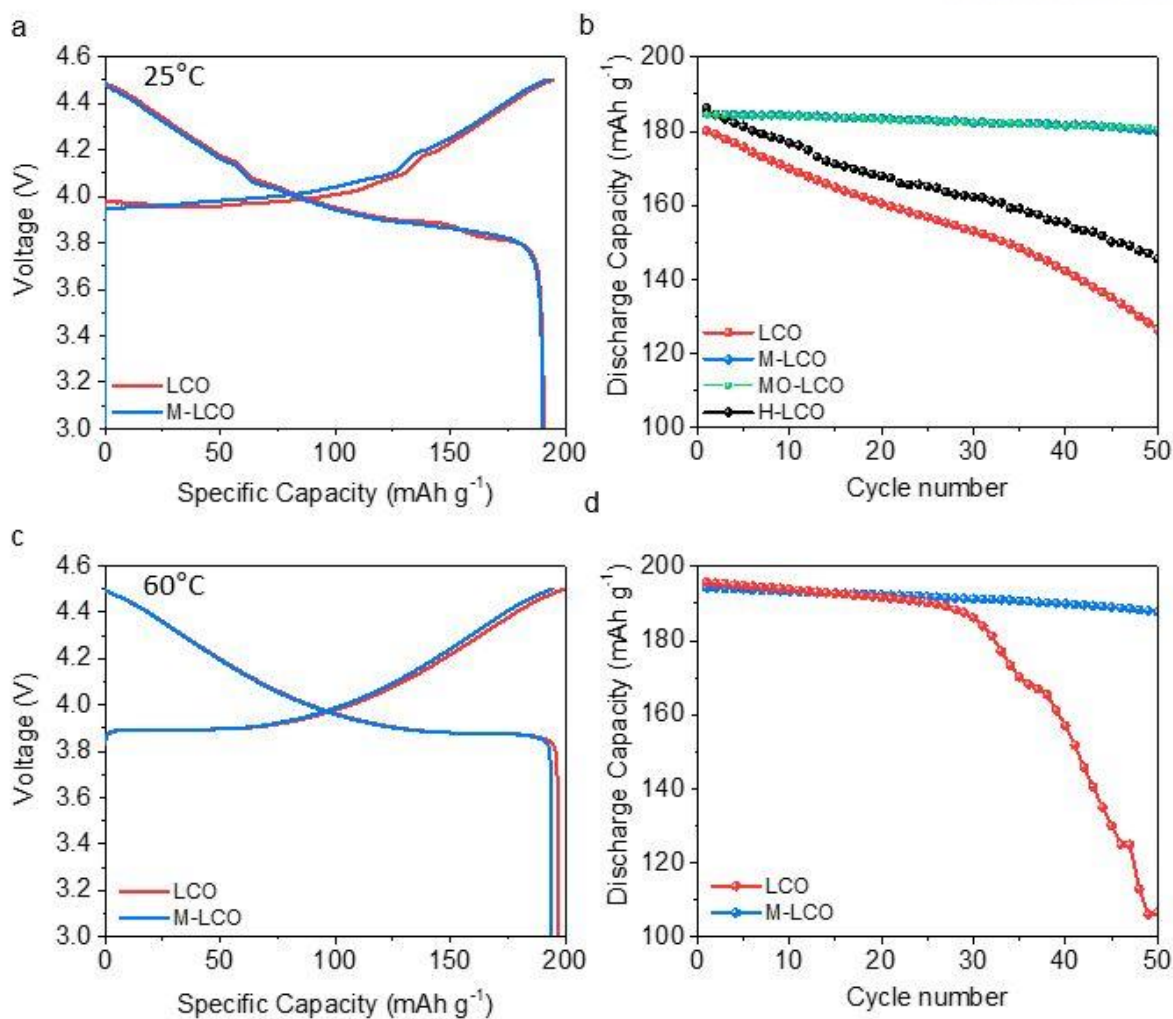


Figure 17. Electrochemical performance (half-cell) of the LCO and M-LCO (voltage range: 3.0 to 4.5 V). (a), (d) The voltage profile graph of the formation cycle at 25 °C and 60 °C. Charge and discharge C-rate was 0.1C. (b), (c) The cycle performance at 25 °C and 60 °C (charge and discharge C-rate: 0.5 and 1C, respectively).

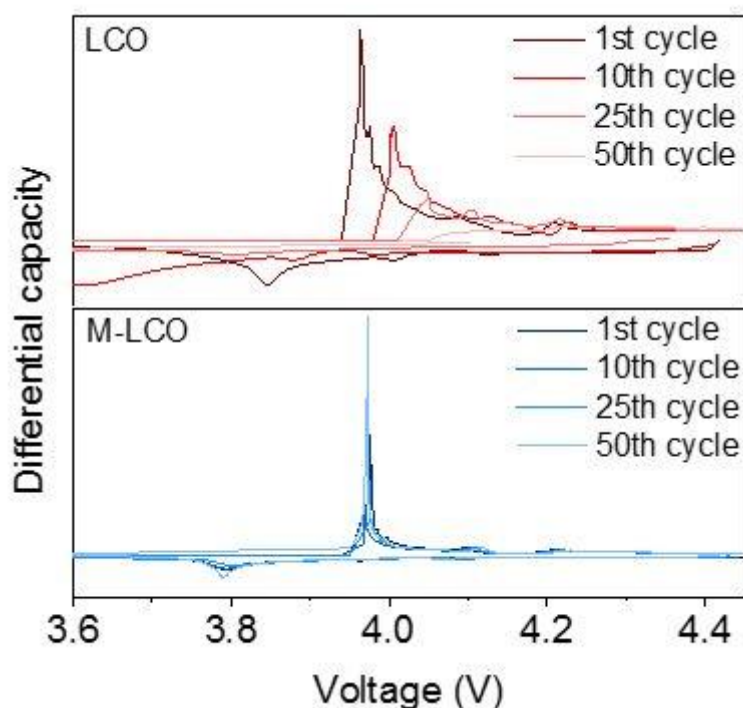


Figure 18. $dq \, dV^{-1}$ curves of 1st, 10th, 25th, 50th cycle for the (a) LCO and (b) M-LCO.

Next, the rate capabilities of the LCO and M-LCO were compared at different discharge C rates ranged from 0.2 to 5.0C and a fixed charge C rate of 0.2C (Figure 19a). The M-LCO showed relatively higher discharge capacity at increased C rates than that of the LCO, indicating that our strategy can enhance the rate capability of the LCO. In particular, the M-LCO retained its initial discharge capacity after the C rate recovered to 0.2 C, while the LCO showed decreased capacity under the same condition. This can be mainly attributed to the intrinsic charge transfer property of cathode materials. Thus, we conducted the EIS analysis to investigate the charge transfer resistance of the LCO and M-LCO (Figure 19b, Table 2). After the formation cycle, the interfacial resistance of the M-LCO was slightly higher than that of the LCO. However, the charge transfer resistance of the M-LCO was stably retained, whereas that of the LCO exhibited a drastic growth during 50 cycles. The incremental resistance in the LCO surface hinders the facile Li-ion transport at the cathode-electrolyte interphase and thereby results in severe capacity fading, as demonstrated in electrochemical results. The enhanced Li ion kinetics at the M-LCO surface was also supported by the GITT results. Figure 20c shows changes in the ohmic potential (IR drop) and overpotential of the LCO and M-LCO during 50 cycles. The values of IR drop and overpotential for the LCO increased approximately 5 times after 50th cycle, whereas no significant change was observed for the M-LCO.

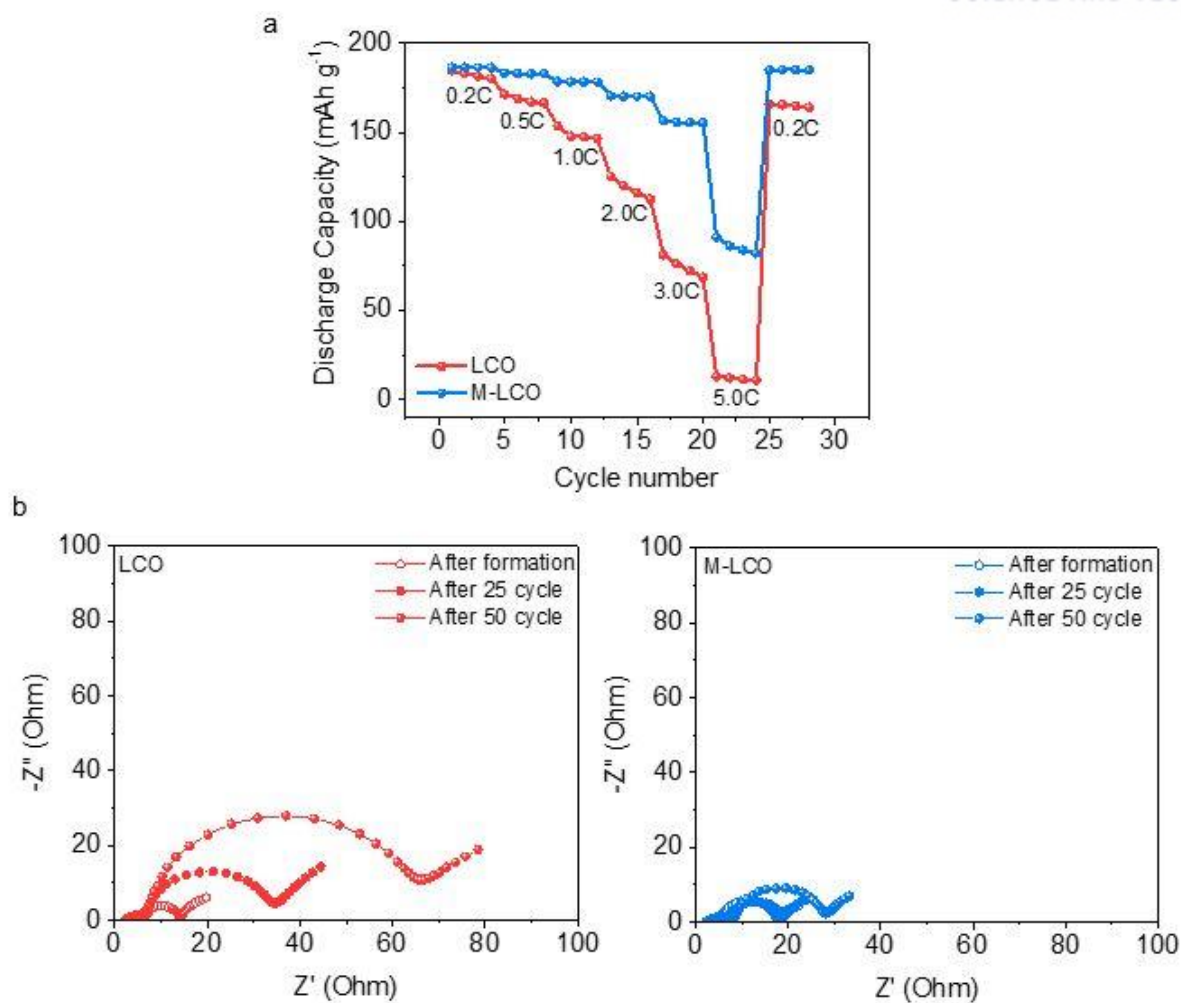


Figure 19. (a) Rate capability test of the LCO and M-LCO. Constant charge C rate (0.2C) was applied and discharge C rate was increased from 0.2 to 5.0C every four cycles. (b) EIS measurements of the LCO and M-LCO recorded after the formation, 25th, and 50th cycle.

Table 2. Charge transfer resistance of the LCO and M-LCO.

Cycle	1 st		25 th		50 th	
Sample	LCO	M-LCO	LCO	M-LCO	LCO	M-LCO
R _{CT} (Ω)	9.2	15.1	31.7	13.3	62.5	23.9

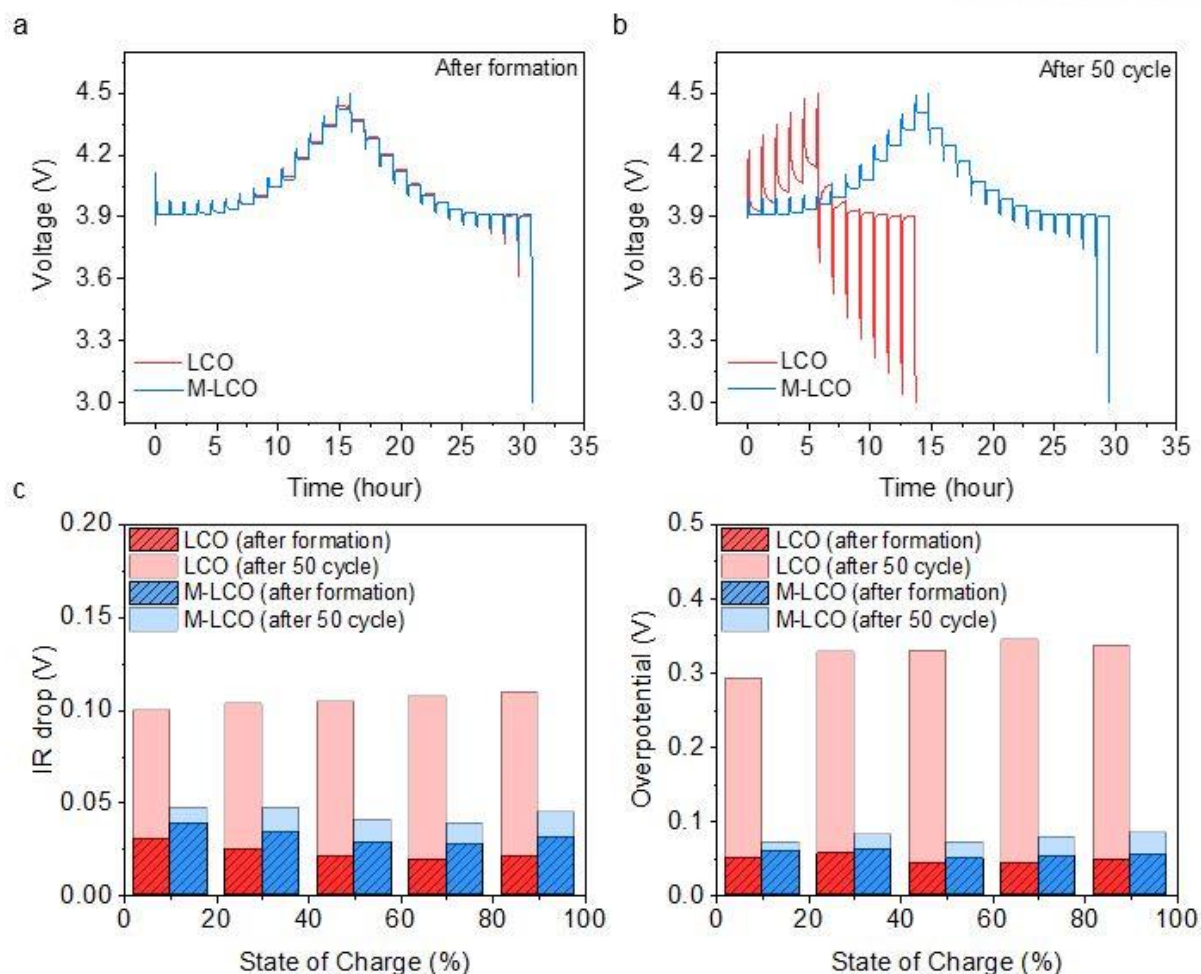


Figure 20. Voltage profile of GITT for the LCO and M-LCO after the (a) formation and (b) 50th cycle. (c) Change in values for IR drop and overpotential at various state of charge (SOC) from 10% to 90%.

To demonstrate the commercial viability of the M-LCO, the full-cell test was conducted with a long-term cycling in the voltage ranged from 2.7 to 4.4 V. A conventional artificial graphite was used for the anode, which shows an initial reversible capacity of $\sim 340 \text{ mAh g}^{-1}$ and stable capacity retention. The LCO/graphite full-cell (LCO/Gr) and M-LCO/graphite full-cell (M-LCO/Gr) delivered initial capacities of 10.8 and 10.3 mAh with initial Coulombic efficiencies of 92.7 and 93.5%, respectively (Figure 21a). In terms of the capacity retention, the M-LCO/Gr exhibited excellent performance of $\sim 87\%$ after 500 cycles, while the LCO/Gr lost almost all initial capacity just after 125 cycles with a dramatically increased overpotential (Figure 21b, d). Furthermore, the M-LCO/Gr showed highly stable retention in the Coulombic efficiency during 500 cycles, compared to that of the LCO/Gr (Figure 21c). Much larger difference in the electrochemical performance was observed in the full-cell system, compared to the half-cell system.

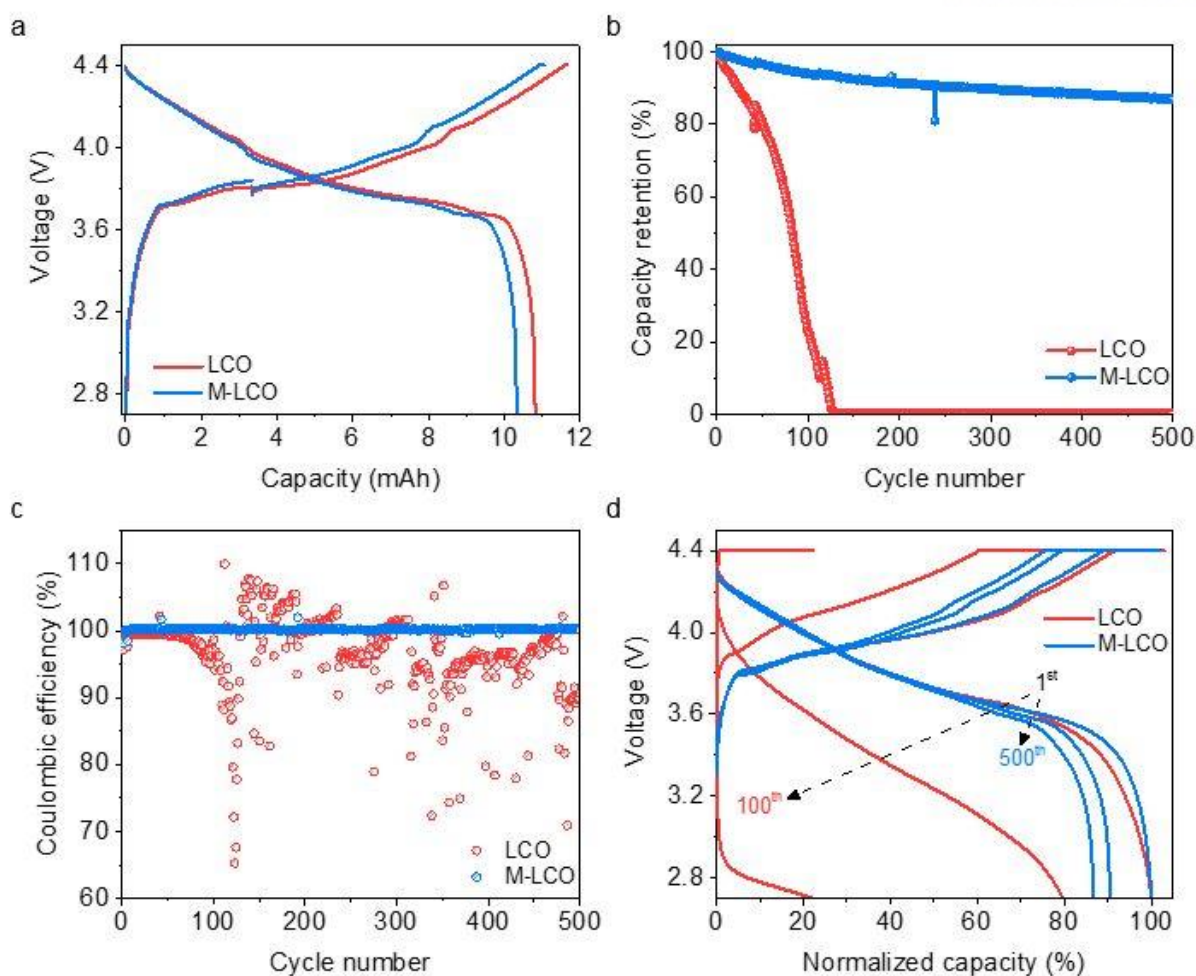


Figure 21. Electrochemical performance of the LCO and M-LCO in the full cell configuration. Artificial graphite was used for the anode. (a) Voltage profile graph at the formation cycle. (b) Cycle performance and (c) coulombic efficiency data during 500 cycles. (d) Change in voltage profile of the LCO and M-LCO during 100 and 500 cycles, respectively.

Co dissolution has been generally accepted as one of the major degradation mechanisms for LCO cathode materials. Accordingly, the LCO and M-LCO electrodes charged to 4.5 V were stored in the electrolyte solution at 60 °C and then the Co content in the solution was investigated by ICP. (Figure 22). As expected, the amount of dissolved Co ions for the LCO electrode was ~2 times larger than that of the M-LCO after 4 weeks. In terms of the loss of Co, more than 7% of Co ions are extracted from the LCO during the storage, which results in the direct loss of the active materials and eventually significant capacity fading (Table 2).

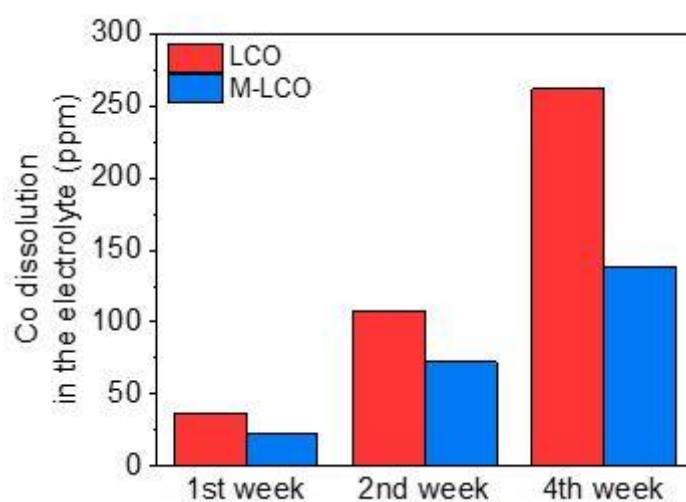


Figure 22. The contents of Co ions in the electrolyte for the LCO and M-LCO after the storage at 60 °C for 4 weeks, measured by ICP.

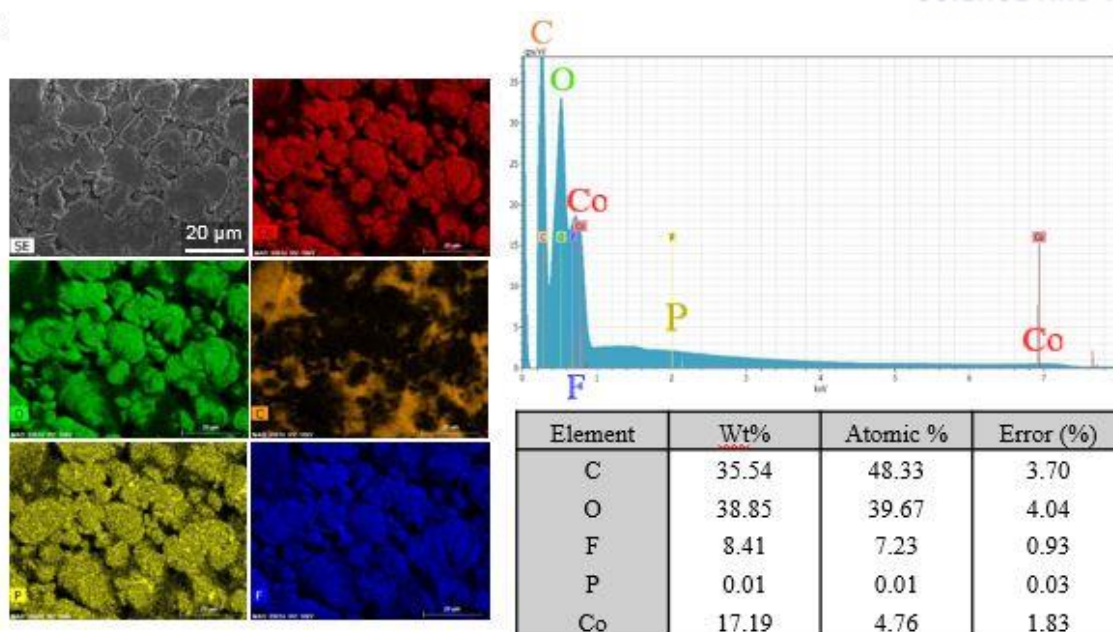
Table 3. Loss of Co from the LCO and M-LCO after storage test.

	Loss of Co (wt%)		
Sample	1 st week	2 nd week	4 th week
LCO	1.06	3.11	7.52
M-LCO	0.66	2.09	3.96

3.3 Structural analysis

To better understand the degradation mechanisms of the LCO/Gr full-cell and the improved electrochemical behavior in the M-LCO/Gr full-cell, we disassembled the cycled full-cells and analyzed each component. Firstly, some in-depth analyses were performed on the LCO and M-LCO cathodes. The SEM-EDX results of LCO and M-LCO surfaces showed that more carbon and fluorine were detected on the LCO cathode surface (Figure 23), which are well-known as decomposition products of the EC solvent and LiPF_6 salt in conventional organic electrolytes.⁶⁰⁻⁶¹ These surface side reactions cause the reduction of TM ions and the formation of disordered phases, which inhibit the diffusion of Li ions at the cathode-electrolyte interphase. Moreover, they consume extra Li ions and the electrolyte, leading to the deterioration in the cell performance. However, considering a huge difference in the capacity retention between the LCO/Gr and M-LCO/Gr full-cell, the variation in detected quantification values for two samples is marginal. Hence, the surface side reactions with the electrolyte is not the main cause of the poor capacity retention in the LCO/Gr full-cell.

a



b

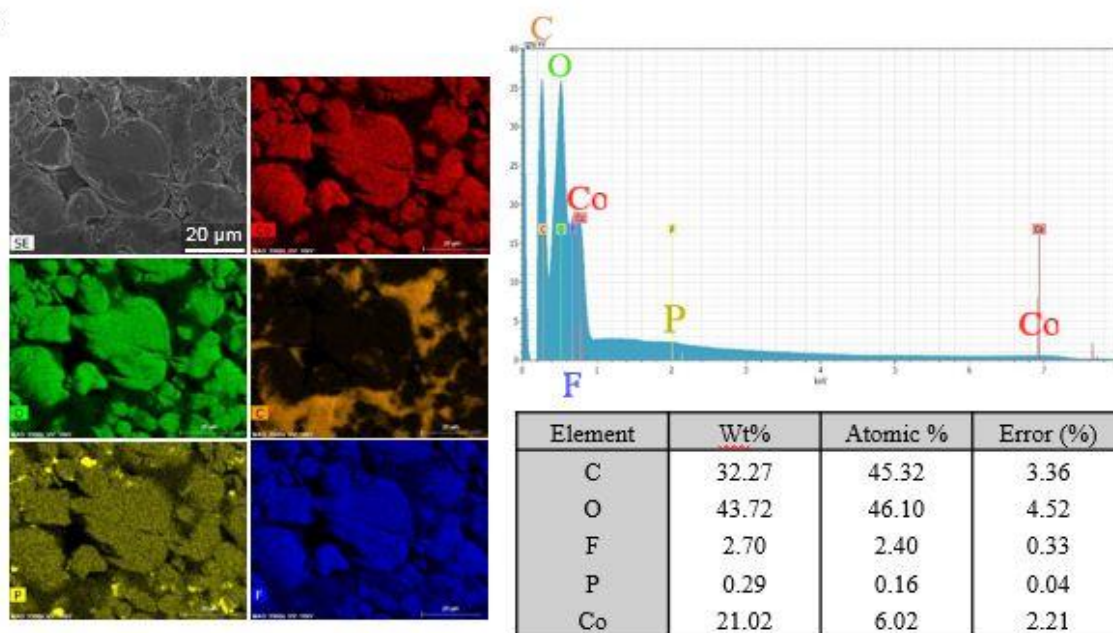
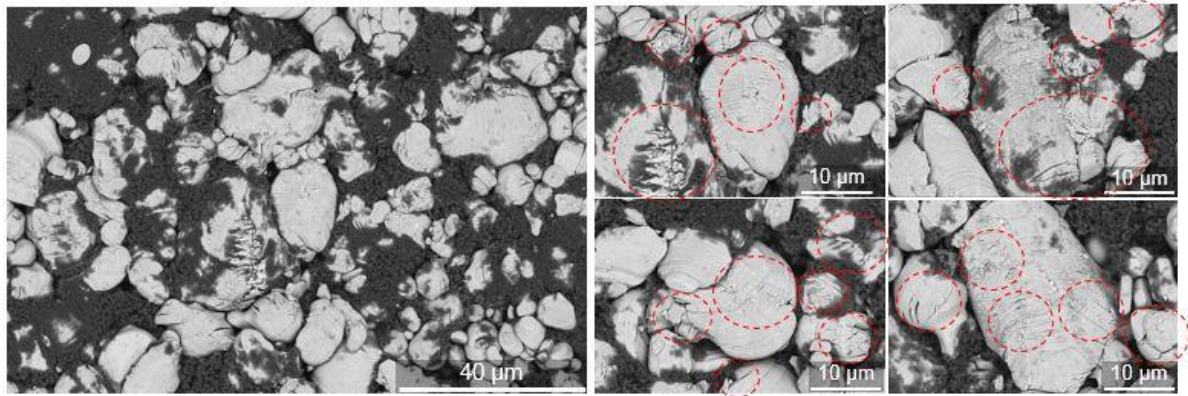


Figure 23. The EDS mapping and spectrum data of the (a) LCO and (b) M-LCO cathode after full-cell test. The quantification data was also included.

Accordingly, to figure out the major degradation mechanism for the LCO/Gr, cathode microstructures in cycled LCO/Gr and M-LCO/Gr full-cells were investigated. As shown in Figure 24, more severe micro-crack generation was observed for the LCO cathode compared to the M-LCO after 500 cycles. Some large cracks segregated one LCO particle into more than two pieces of particles, which was mainly observed in the large-sized LCO particle. Centered on these large cracks, many smaller cracks were formed in the LCO particle. Some large micro-cracks were also observed in the M-LCO particle, but small crack formation was noticeably mitigated (Figure 24b). HR-TEM analysis showed more clear differences in micro- and atomic-scale structure between the LCO and M-LCO particles. As expected, severe crack formation was apparently observed both on the surface and inside the LCO cathode particles compared to the M-LCO particles (Figure 25a, 26a). Notably, the newly formed cracks within the LCO particle would be exposed to the electrolyte, which may cause additional side reactions and consequent phase transition as well as TM reduction inside the particle. This leads to the drastic internal resistance growth and eventually deteriorates the electrochemical performances of the cathode.

On the other hand, the M-LCO retained its smooth and even surface after the full-cell 500 cycles, whereas the LCO has a relatively uneven surface (Figure 25b, 26b). The difference in the uniformity between two cathode surfaces may be attributed to the suppression of the crack formation and Co dissolution as a result of the introduction of the Mg ions into the LCO surface. After cycling, the LCO surface underwent a phase transition from the layered structure to the spinel and rock salt structure (~ 2 nm), as evidenced by the HAADF-STEM image and FFT patterns of the LCO surface (Figure 25c). Pit formation was also observed near the outermost surface of the LCO, which may be originated from the Co dissolution. However, the inside of the outermost LCO surface was appeared to retain original layered structure after 500 cycles. This implies that the surface damage of the LCO cathode was not too severe considering the highly poor capacity retention of the LCO/Gr full-cell, which corresponds to the EDX results. Therefore, it is worth mentioning that the drastic capacity fading of the large-sized LCO cathode was mainly due to the severe crack formation. In contrast, there was no significant change in the M-LCO surface during cycling. Hence, we could conclude that the introduction of the Mg ions into the LCO surface enhances the structural and chemical stability of the LCO surface by forming $\text{LiMg}_x\text{Co}_{1-x}\text{O}_2$ ($x < 1$) phase.⁴⁹

a



b

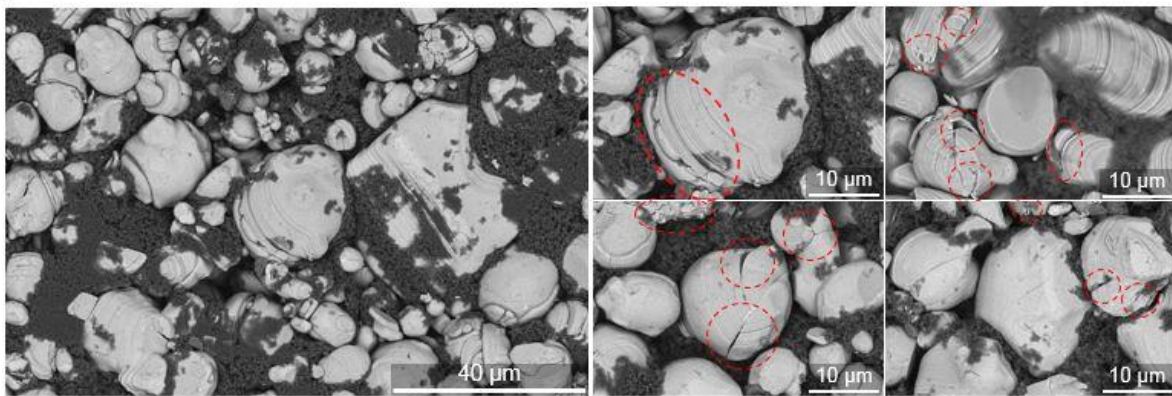


Figure 24. SEM images of the (a) LCO and (b) M-LCO cathode composite after full cell 500 cycles.

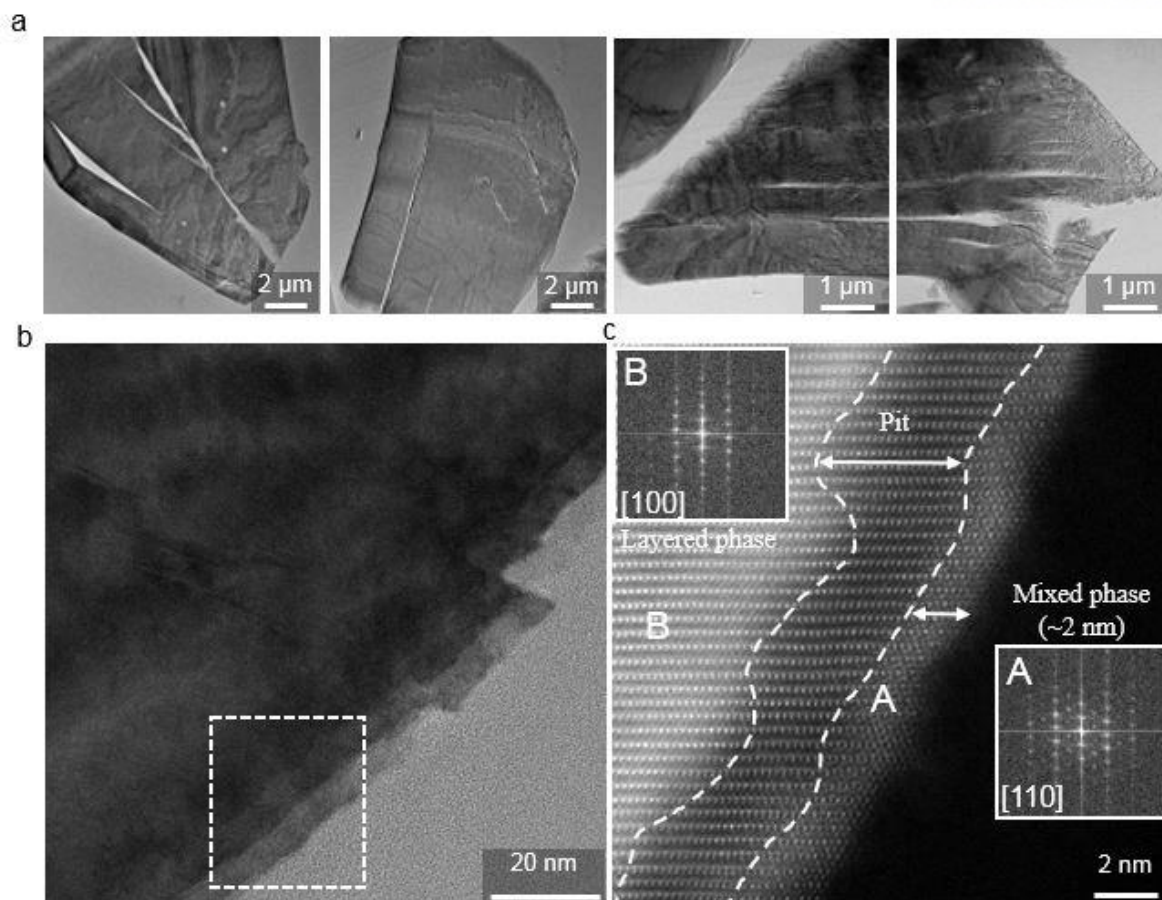


Figure 25. Micro and atomic structure of the LCO surface after cycling. (a) TEM images of the LCO after full-cell 500 cycles. (b) A HR-TEM image of the LCO surface. (c) A STEM image of the white box in (b). The insets are FFT patterns of the region 'A' and 'B'.

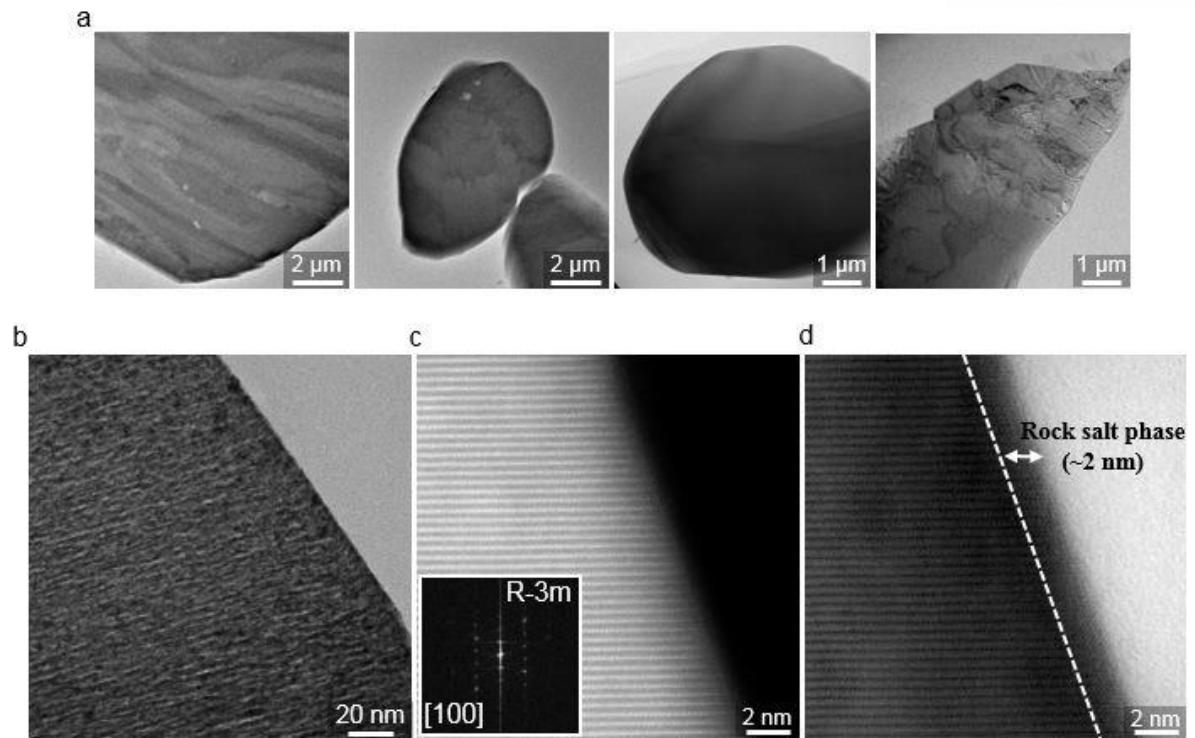


Figure 26. Surface micro and atomic structure of the M-LCO after cycling. (a) TEM images of the M-LCO after full-cell 50 cycles. (b) A HR-TEM image of the M-LCO surface. (c) Outermost STEM image in (b). The inset is the FFT pattern of the surface in (c). (d) A bright-field (BF) STEM image of the (c).

Figure 27 shows separated LCO particles by a large micro-crack formation after 500 cycles. As observed in SEM images, some small cracks were generated near the large crack. Interestingly, two separated LCO particles have different crystallographic orientations each other (Figure 27c). In fact, some large-sized pristine LCO consisted of several medium-sized LCO particles, forming a large secondary particle. Accordingly, different crystallographic orientations have existed in one particle before cycling. Therefore, continuous charging and discharging process could result in the anisotropic expansion and shrinkage of each primary particle, inducing significant strains and eventually crack generation at the grain boundary. A magnified HR-TEM image in Figure 28b shows some small cracks inside the LCO particle. As shown in STEM images, TM layers near the small crack significantly bent owing to the strain (Figure 28c, d). This continuous strain would break the TM-TM bonds and inevitably form other cracks. Furthermore, rock salt phase formation was also observed near the cracks, which is consistent with a recent study (Figure 28e, f).⁴⁵ This phase transition is accompanied by the oxygen evolution from the LCO lattice and inhibits the reversible intercalation and deintercalation of Li ions near the crack. Therefore, we could conclude that the severe deterioration of the electrochemical performance in the LCO cathode is originated from the significant damage in the micro- and nanostructure. This detrimental structural damage can be suppressed by the incorporation of the Mg ions into the LCO structure. Magnesium ions substitute the Co or Li sites and function as a pillar which can maintain the TM-O bond even in the highly delithiated state. This results in the suppression of the structural collapse and crack formation, leading to the excellent capacity retention of the M-LCO. The improved structural stability of the M-LCO is also supported by the XRD data. Figure 29 shows the change in XRD peaks of the LCO and M-LCO after cycling. Notably, significant broadening and shift of the (003) peak at $\sim 19^\circ$ was observed for the LCO, which implies that the distance between two TM layers considerably increased. In addition, some peak changes including the disappearance of the (006) peak demonstrated the severe structural change of the LCO. In stark contrast, the M-LCO showed a little peak shift, but retained the original structure during cycling.

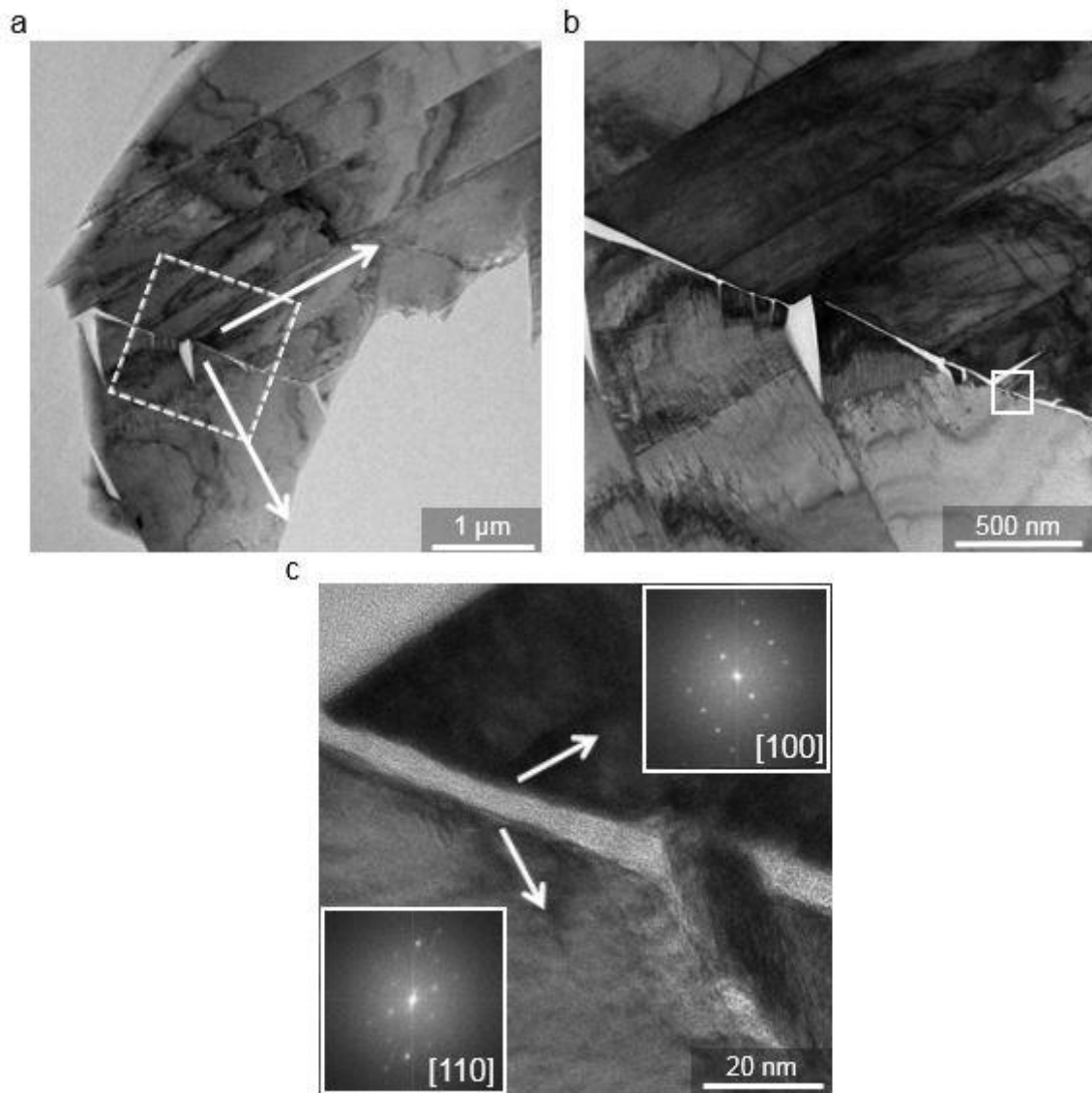


Figure 27. (a) A TEM image showing the large microcrack in the cycled LCO. (b) A magnified TEM image of the white box in (a). (c) A magnified HR-TEM image of the white box in (b). The white arrows indicate different Li ion diffusion pathway in each broken particle. The insets are FFT patterns from each separated particle.

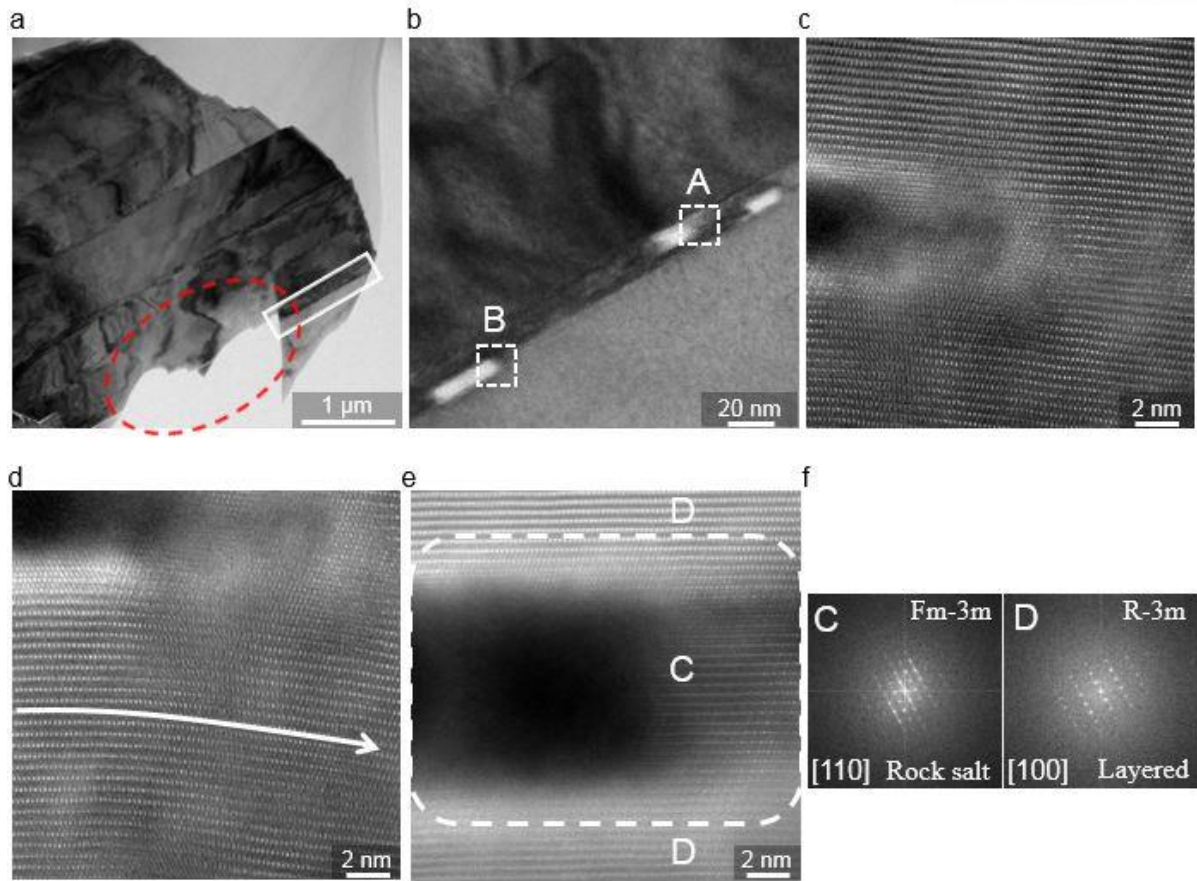


Figure 28. Micro and atomic structure of the LCO near the cracks. (a) A TEM image of the LCO after cycling. The red ellipse indicates the broken interface of the particle that the crack formed. (b) A HR-TEM image of the white box in (a). (c), (d) STEM images of the white box 'A' in (b). (e) A STEM image of the white box 'B' in (b). (f) FFT patterns in region 'C' and 'D' in (e).

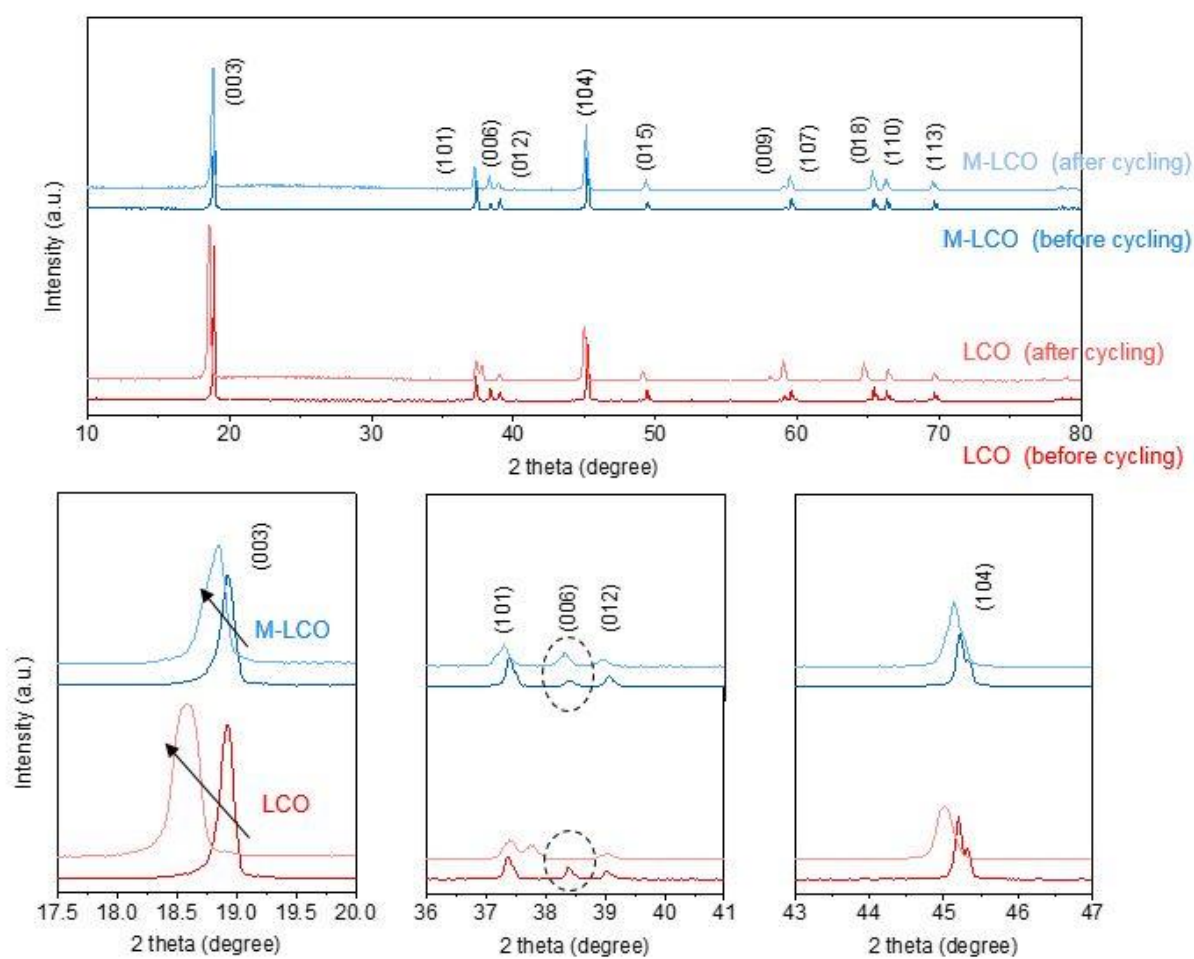


Figure 29. Change in XRD peaks of the LCO and M-LCO after cycling.

As mentioned in Part 1.2.3, there have been no direct evidence demonstrating that the Co ion crossover causes the capacity fading of the anode and LCO/Gr full-cell. Thus, we observed the anode surface of the disassembled LCO/Gr and M-LCO/Gr full-cell in order to investigate the effect of the Co ion crossover on the full-cells (Figure 30). The back-scattered electrons (BSE)-SEM images enabled a clear identification of the cobalt on the graphite anode, as relatively heavier element appears white in this mode. As evidenced by the BSE-SEM and EDX analysis, the Co ions were deposited on the anode surface of the LCO/Gr full-cell, whereas hardly found on the anode surface of the M-LCO/Gr full-cell (Figure 30a, b). In fact, the amount of deposited Co ions on the anode of the LCO/Gr full-cell was approximately 1% to that of carbon (Figure 31a). To validate the effect of the Co ion crossover on the anode and full-cell degradation, disassembled LCO/Gr and M-LCO/Gr full-cells were reassembled into the coin type half-cells using the used cathode and anode with a fresh Li metal and electrolyte. The reassembled half-cells were charged and discharged for 25 cycles at a low C rate of 0.1C with a voltage ranged from 0.005 to 1.5 V for the anode and from 3.0 to 4.5 V for the cathode half-cells in order to confirm the reversible capacity. Interestingly, after the first cycle, the capacity of both anodes from LCO/Gr and M-LCO/Gr full-cells was recovered to $\sim 300 \text{ mAh g}^{-1}$ and stably retained this capacity during 25 cycles (Figure 32). Considering the used graphite anode has a reversible capacity of $\sim 340 \text{ mAh g}^{-1}$, approximately 88% of initial capacity was obtained in two anodes even after the 500 cycles in the high voltage condition. This apparently demonstrates that the Co ion crossover on the anode surface hardly affects the capacity fading of the graphite anode and LCO/Gr full-cell. Furthermore, we could conclude that the severe capacity fading in the LCO/Gr full-cell was mainly originated from the cathode degradation, as the anode of the LCO/Gr had similar capacity with that of the M-LCO/Gr full-cell after the reassembly. The electrochemical cycling data from reassembled cathode half-cells also supported our conclusion. The reassembled cathode of LCO/Gr full-cell had a initial capacity of $\sim 98 \text{ mAh g}^{-1}$, which is a half of the original reversible capacity of the LCO. Furthermore, the pristine LCO cathode showed a high overpotential and drastic capacity fading during 25 cycles, despite the low-rate cycles of 0.1C. However, the reassembled M-LCO cathode almost completely recovered original reversible capacity and showed stable capacity retention during 25 cycles.

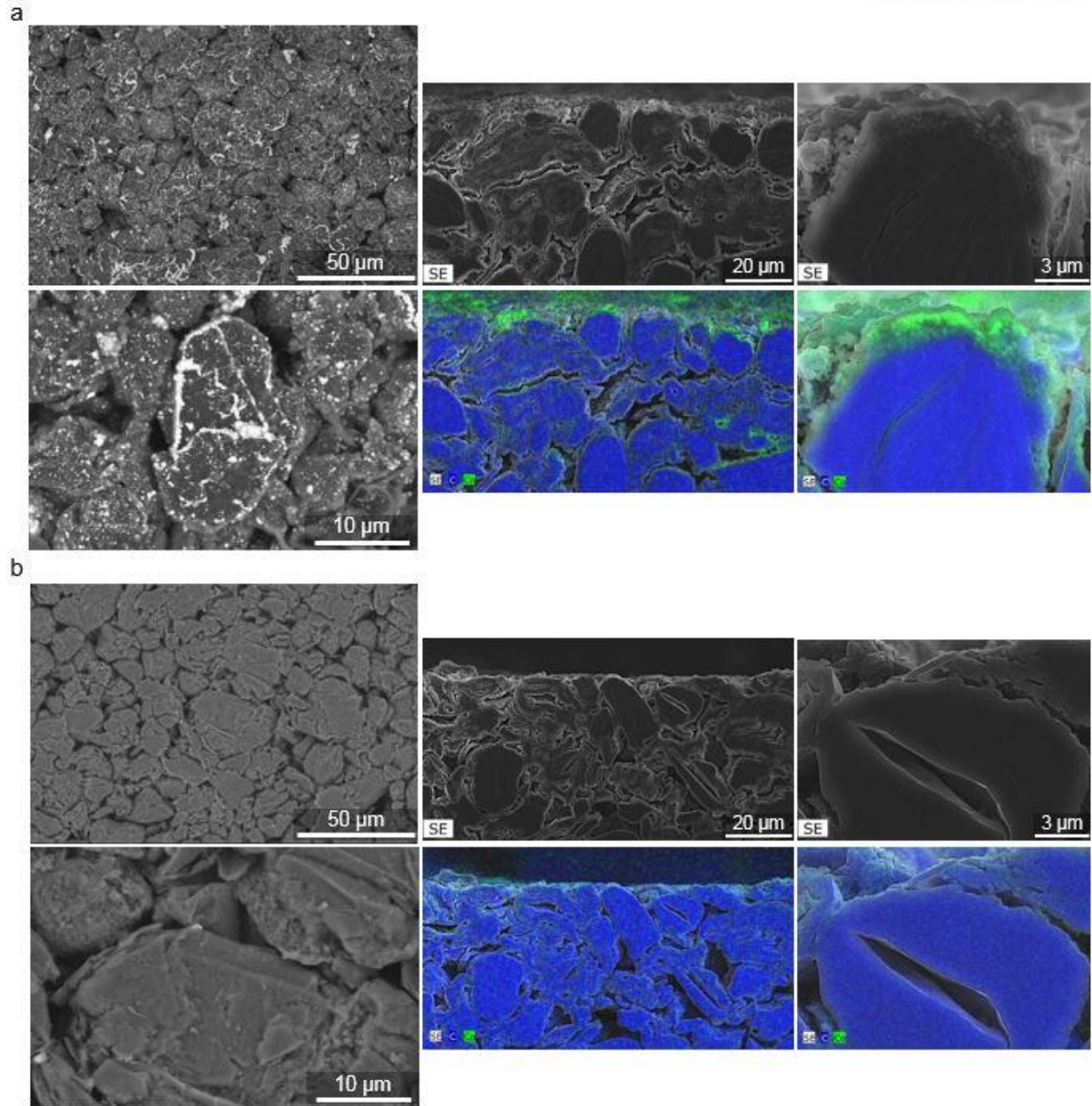
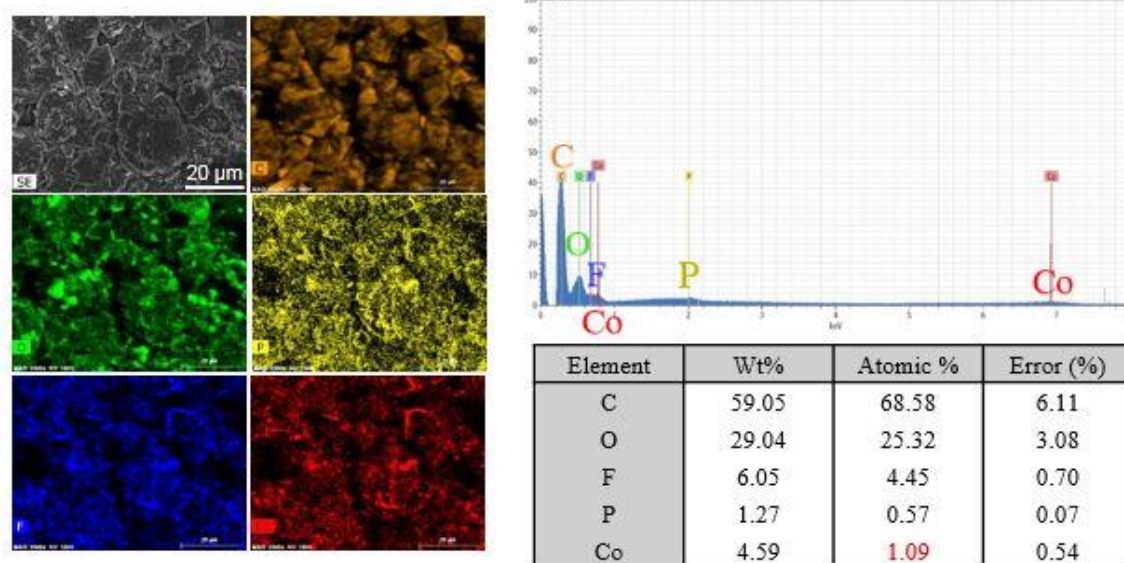


Figure 30. The SEM images of the graphite anode in the (a) LCO/Gr and (b) M-LCO/Gr full cell after 500 cycles. The cross-sectional SEM images and EDS mapping data (right side) was presented. In the mapping image, blue and green signals indicate the carbon and cobalt element, respectively.

a



b

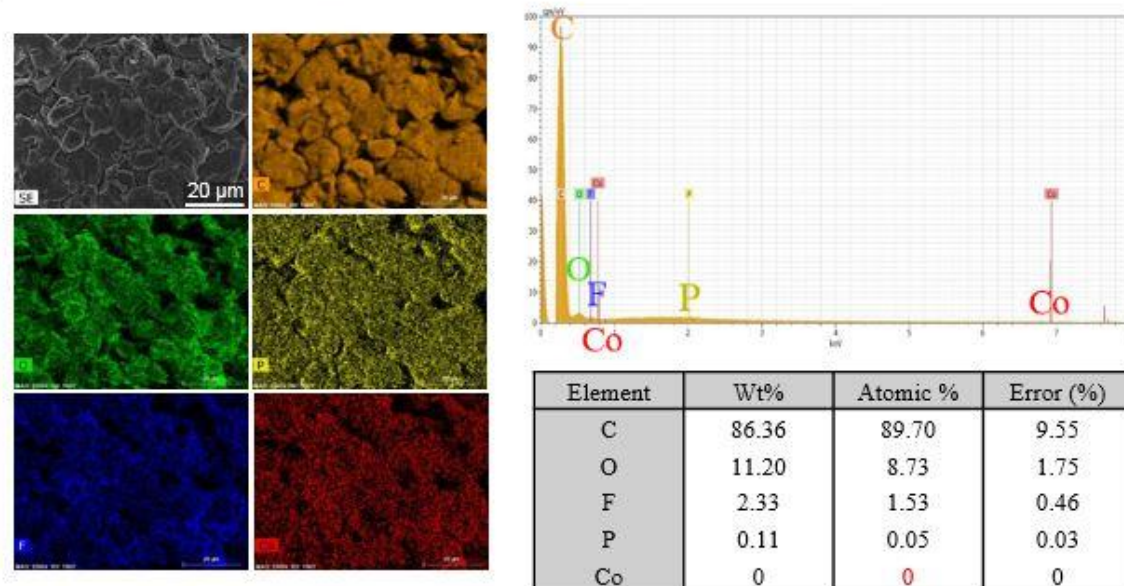


Figure 31. The EDS mapping and spectrum data of the graphite anode in the (a) LCO/Gr and (b) M-LCO/Gr full cell after the 500 cycles. The quantification data was also presented.

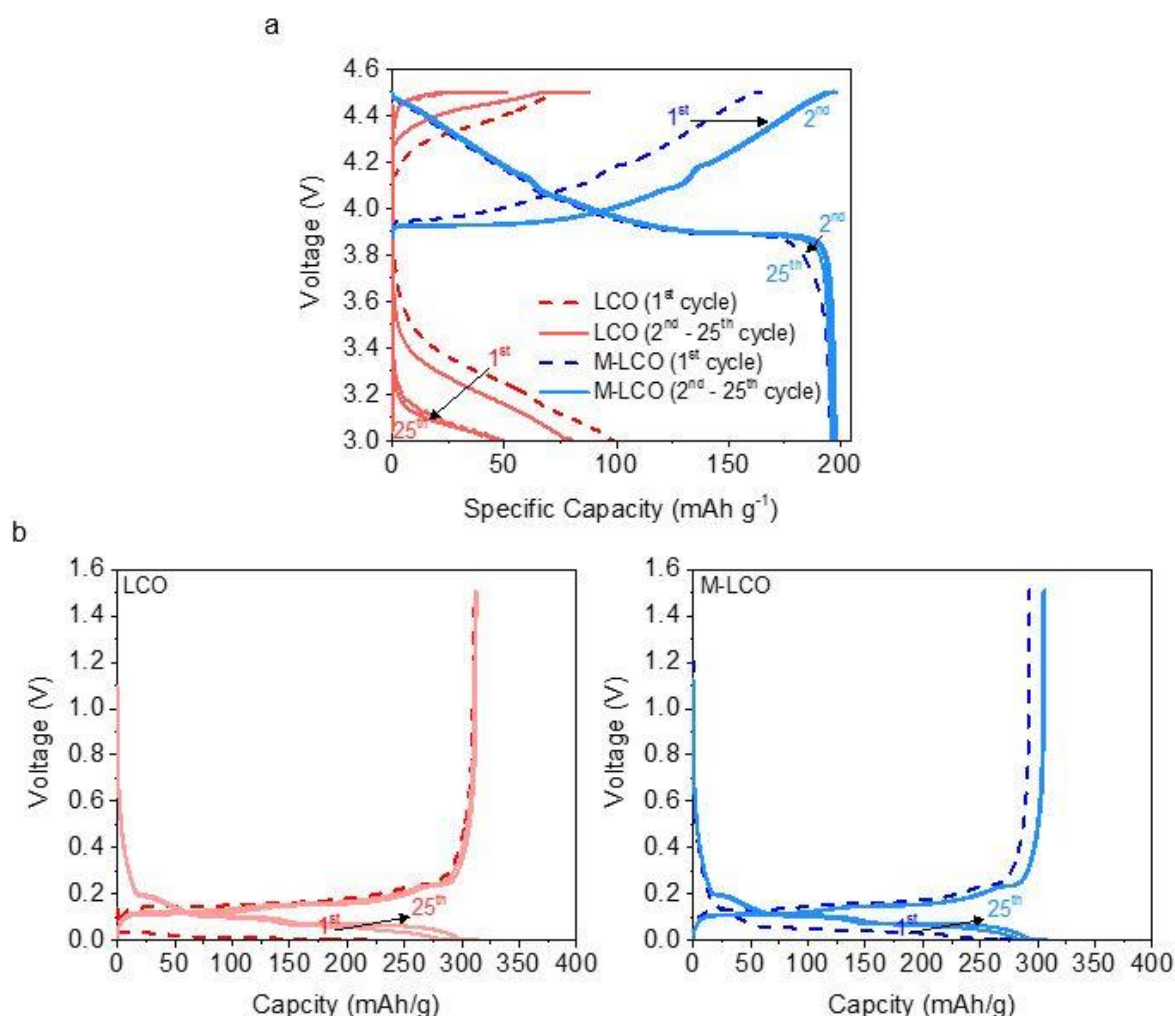


Figure 32. (a) Voltage profiles of the reassembled LCO and M-LCO cathode in half-cell after full-cell 500 cycles (voltage range: 3.0 to 4.5 V). (b) Voltage profiles of the reassembled graphite anode half-cell in the voltage ranged from 0.005 to 1.5 V. Fresh electrolyte and lithium metal were used for the reassembly and all the reassembled half-cells were charged and discharged 25 times at 0.1C.

Finally, the surface of separators used in the LCO/Gr and M-LCO/Gr full cells was investigated through the SEM-EDX analysis. The severe clogging of the pores and the accumulation of surface deposits were observed in the LCO/Gr separator (Figure 33a, b). Previous studies reported that side reactions on both electrode surfaces and decomposition of the electrolyte at high voltages can produce the undesirable surface deposits on the separator surface.⁶²⁻⁶³ This could cause the porosity loss and decline in ionic conductivity of the separator, resulting in high overpotential. Furthermore, blocking of pores impede homogeneous current distribution and induce the formation of Li dendrite on the anode surface, which eventually leads to the failure of the full-cell. On the contrary, the M-LCO/Gr separator had a clean surface and unclogged pores after cycling, which may be ascribed to decreased

side reactions at both electrodes. Reduced cracking in the M-LCO cathode may suppress the additional electrolyte decomposition at new surfaces derived from the cracks, and thereby affect to decreased side reaction products on the surface of the anode and separator. This result elucidates that the significant difference in the electrochemical performance between the LCO/Gr and M-LCO/Gr full-cell was partly attributed to the poor Li ion diffusivity in the LCO/Gr separator.

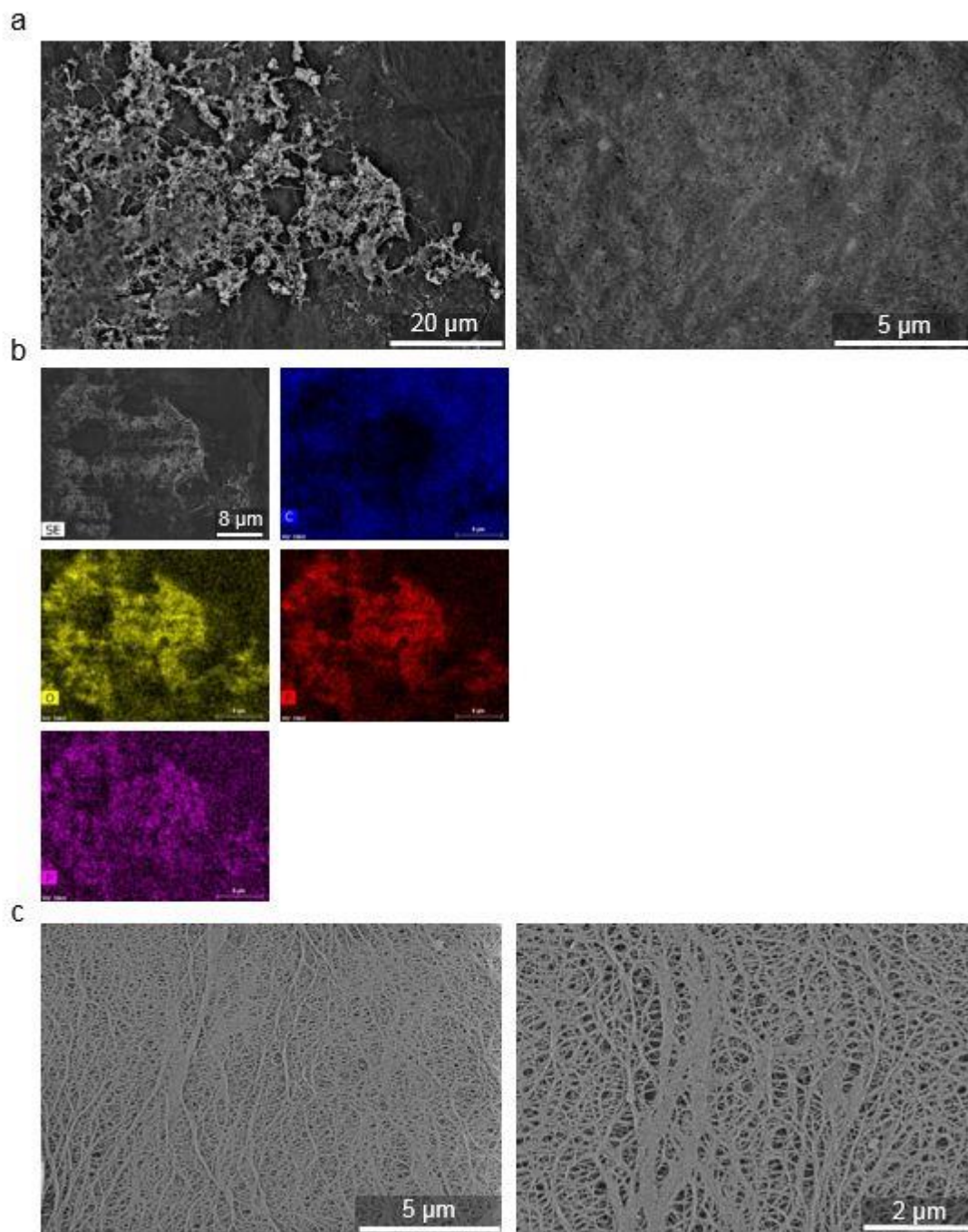


Figure 33. The SEM images (BSE mode) of the separator in the (a) LCO/Gr and (c) M-LCO/Gr full-cell after the 500 cycles. (b) EDS mapping image for the separator in the LCO/Gr full cell.

4. Conclusion

This work has demonstrated the major degradation mechanism of the large-sized LCO at high voltage of 4.5 V (vs Li/Li⁺) by investigating each component of the LCO/Gr full-cell after 500 cycles. The severe degradation of the LCO/Gr full-cell was mainly due to the severe irreversible structural change and crack formation. Notably, severe crack generation can continuously expose a new surface to the electrolyte, which gives rise to the additional side reactions consuming extra Li ions and eventually leads to the drastic internal resistance growth within the cell. Interestingly, the side reactions on the LCO cathode surface and Co ion crossover on the anode surface do not significantly affect the electrochemical performance of the cathode and anode, which is not consistent with previous studies. Furthermore, we suggested the high temperature solid-state surface modification using the magnesium phosphate as one of the powerful methods to enable the high-voltage operation of the LCO cathode. The modified M-LCO showed Mg gradient from the surface, which exhibited significantly enhanced the reversibility of structural change and morphological robustness. Besides the bulk properties, our simple method improved the surface stability of the LCO, thereby showing the dual effect of the surface coating and bulk doping. This led to the significantly improved electrochemical performance of the LCO cathode especially in the full-cell system, which can meet the high level of commercial standard in LIBs.

References

1. Ibrahim, H.; Ilinca, A.; Perron, J., Energy storage systems—Characteristics and comparisons. *Renewable and Sustainable Energy Reviews* **2008**, *12* (5), 1221-1250.
2. Cho, J.; Jeong, S.; Kim, Y., Commercial and research battery technologies for electrical energy storage applications. *Progress in Energy and Combustion Science* **2015**, *48*, 84-101.
3. Larcher, D.; Tarascon, J. M., Towards greener and more sustainable batteries for electrical energy storage. *Nature Chemistry* **2014**, *7*, 19.
4. Whittingham, M. S., Lithium Batteries and Cathode Materials. *Chemical Reviews* **2004**, *104* (10), 4271-4302.
5. Ohzuku, T.; Ueda, A., Solid-State Redox Reactions of LiCoO₂ (R $\bar{3}$ m) for 4 Volt Secondary Lithium Cells. *Journal of The Electrochemical Society* **1994**, *141* (11), 2972-2977.
6. Cho, J.; Kim, Y. J.; Park, B., LiCoO₂ Cathode Material That Does Not Show a Phase Transition from Hexagonal to Monoclinic Phase. *Journal of The Electrochemical Society* **2001**, *148* (10), A1110-A1115.
7. Amatucci, G. G.; Tarascon, J. M.; Klein, L. C., Cobalt dissolution in LiCoO₂-based non-aqueous rechargeable batteries. *Solid State Ionics* **1996**, *83* (1), 167-173.
8. Kim, Y. J.; Cho, J.; Kim, T.-J.; Park, B., Suppression of Cobalt Dissolution from the LiCoO₂ Cathodes with Various Metal-Oxide Coatings. *Journal of The Electrochemical Society* **2003**, *150* (12), A1723-A1725.
9. Gabrisch, H.; Yazami, R.; Fultz, B., Hexagonal to Cubic Spinel Transformation in Lithiated Cobalt Oxide: TEM Investigation. *Journal of The Electrochemical Society* **2004**, *151* (6), A891-A897.
10. Kikkawa, J.; Terada, S.; Gunji, A.; Nagai, T.; Kurashima, K.; Kimoto, K., Chemical States of Overcharged LiCoO₂ Particle Surfaces and Interiors Observed Using Electron Energy-Loss Spectroscopy. *The Journal of Physical Chemistry C* **2015**, *119* (28), 15823-15830.
11. Sun, Y. K.; Han, J. M.; Myung, S. T.; Lee, S. W.; Amine, K., Significant improvement of high voltage cycling behavior AlF₃-coated LiCoO₂ cathode. *Electrochemistry Communications* **2006**, *8* (5), 821-826.
12. Lu, Y.-C.; Mansour, A. N.; Yabuuchi, N.; Shao-Horn, Y., Probing the Origin of Enhanced Stability of “AlPO₄” Nanoparticle Coated LiCoO₂ during Cycling to High Voltages: Combined XRD and XPS Studies. *Chemistry of Materials* **2009**, *21* (19), 4408-4424.
13. Seong, W. M.; Yoon, K.; Lee, M. H.; Jung, S.-K.; Kang, K., Unveiling the Intrinsic Cycle Reversibility of a LiCoO₂ Electrode at 4.8-V Cutoff Voltage through Subtractive Surface Modification for Lithium-Ion Batteries. *Nano Letters* **2018**.
14. Bruno G. A. Freitas, J. M. S. J., Leonardo M. da Costa, Glaucio B. Ferreira and Jackson A. L. C. Resende, Synthesis and Characterization of LiCoO₂ from Different Precursors by Sol-Gel Method. *J. Braz. Chem. Soc.* **2017**, *28* (11), 2254-2266.
15. Kalluri, S.; Yoon, M.; Jo, M.; Park, S.; Myeong, S.; Kim, J.; Dou, S. X.; Guo, Z.; Cho, J., Surface Engineering Strategies of Layered LiCoO₂ Cathode Material to Realize High-Energy and High-Voltage Li-Ion Cells. *Advanced Energy Materials* **2017**, *7* (1), 1601507-n/a.
16. Li, W.; Song, B.; Manthiram, A., High-voltage positive electrode materials for lithium-ion batteries. *Chemical Society Reviews* **2017**, *46* (10), 3006-3059.

17. Goodenough, J. B.; Kim, Y., Challenges for Rechargeable Li Batteries. *Chemistry of Materials* **2010**, 22 (3), 587-603.
18. Verma, P.; Maire, P.; Novák, P., A review of the features and analyses of the solid electrolyte interphase in Li-ion batteries. *Electrochimica Acta* **2010**, 55 (22), 6332-6341.
19. Goodenough, J. B.; Park, K.-S., The Li-Ion Rechargeable Battery: A Perspective. *Journal of the American Chemical Society* **2013**, 135 (4), 1167-1176.
20. Yano, A.; Shikano, M.; Ueda, A.; Sakaebe, H.; Ogumi, Z., LiCoO₂ Degradation Behavior in the High-Voltage Phase Transition Region and Improved Reversibility with Surface Coating. *Journal of The Electrochemical Society* **2017**, 164 (1), A6116-A6122.
21. Yang, Z.; Li, R.; Deng, Z., A deep study of the protection of Lithium Cobalt Oxide with polymer surface modification at 4.5 V high voltage. *Scientific Reports* **2018**, 8 (1), 863.
22. Gauthier, M.; Carney, T. J.; Grimaud, A.; Giordano, L.; Pour, N.; Chang, H.-H.; Fenning, D. P.; Lux, S. F.; Paschos, O.; Bauer, C.; Maglia, F.; Lupart, S.; Lamp, P.; Shao-Horn, Y., Electrode–Electrolyte Interface in Li-Ion Batteries: Current Understanding and New Insights. *The Journal of Physical Chemistry Letters* **2015**, 6 (22), 4653-4672.
23. Sloop, S. E.; Kerr, J. B.; Kinoshita, K., The role of Li-ion battery electrolyte reactivity in performance decline and self-discharge. *Journal of Power Sources* **2003**, 119-121, 330-337.
24. Krueger, S.; Klopsch, R.; Li, J.; Nowak, S.; Passerini, S.; Winter, M., How Do Reactions at the Anode/Electrolyte Interface Determine the Cathode Performance in Lithium-Ion Batteries? *Journal of The Electrochemical Society* **2013**, 160 (4), A542-A548.
25. Takamatsu, D.; Koyama, Y.; Orikasa, Y.; Mori, S.; Nakatsutsumi, T.; Hirano, T.; Tanida, H.; Arai, H.; Uchimoto, Y.; Ogumi, Z., First In Situ Observation of the LiCoO₂ Electrode/Electrolyte Interface by Total-Reflection X-ray Absorption Spectroscopy. *Angewandte Chemie International Edition* **2012**, 51 (46), 11597-11601.
26. Teshager, M. A.; Lin, S. D.; Hwang, B.-J.; Wang, F.-M.; Hy, S.; Haregewoin, A. M., In Situ DRIFTS Analysis of Solid-Electrolyte Interphase Formation on Li-Rich Li_{1.2}Ni_{0.2}Mn_{0.6}O₂ and LiCoO₂ Cathodes during Oxidative Electrolyte Decomposition. *ChemElectroChem* **2016**, 3 (2), 337-345.
27. Wang, J.; Ji, Y.; Appathurai, N.; Zhou, J.; Yang, Y., Nanoscale chemical imaging of the additive effects on the interfaces of high-voltage LiCoO₂ composite electrodes. *Chemical Communications* **2017**, 53 (61), 8581-8584.
28. Jarry, A.; Gottis, S.; Yu, Y.-S.; Roque-Rosell, J.; Kim, C.; Cabana, J.; Kerr, J.; Kostecki, R., The Formation Mechanism of Fluorescent Metal Complexes at the Li_xNi_{0.5}Mn_{1.5}O₄-δ/Carbonate Ester Electrolyte Interface. *Journal of the American Chemical Society* **2015**, 137 (10), 3533-3539.
29. Vissers, D. R.; Chen, Z.; Shao, Y.; Engelhard, M.; Das, U.; Redfern, P.; Curtiss, L. A.; Pan, B.; Liu, J.; Amine, K., Role of Manganese Deposition on Graphite in the Capacity Fading of Lithium Ion Batteries. *ACS Applied Materials & Interfaces* **2016**, 8 (22), 14244-14251.
30. Zhan, C.; Wu, T.; Lu, J.; Amine, K., Dissolution, migration, and deposition of transition metal ions in Li-ion batteries exemplified by Mn-based cathodes - a critical review. *Energy & Environmental Science* **2018**, 11 (2), 243-257.

31. Thackeray, M. M.; Johnson, P. J.; de Picciotto, L. A.; Bruce, P. G.; Goodenough, J. B., Electrochemical extraction of lithium from LiMn_2O_4 . *Materials Research Bulletin* **1984**, *19* (2), 179-187.
32. Aurbach, D.; Markovsky, B.; Salitra, G.; Markevich, E.; Talyossef, Y.; Koltypin, M.; Nazar, L.; Ellis, B.; Kovacheva, D., Review on electrode–electrolyte solution interactions, related to cathode materials for Li-ion batteries. *Journal of Power Sources* **2007**, *165* (2), 491-499.
33. Kim, J.; Ma, H.; Cha, H.; Lee, H.; Sung, J.; Seo, M.; Oh, P.; Park, M.; Cho, J., A highly stabilized nickel-rich cathode material by nanoscale epitaxy control for high-energy lithium-ion batteries. *Energy & Environmental Science* **2018**.
34. Li, B.; Wang, Y.; Lin, H.; Liu, J.; Xing, L.; Xu, M.; Li, W., Improving high voltage stability of lithium cobalt oxide/graphite battery via forming protective films simultaneously on anode and cathode by using electrolyte additive. *Electrochimica Acta* **2014**, *141*, 263-270.
35. Van der Ven, A.; Aydinol, M. K.; Ceder, G., First-Principles Evidence for Stage Ordering in Li_xCoO_2 . *Journal of The Electrochemical Society* **1998**, *145* (6), 2149-2155.
36. Chen, Z.; Dahn, J. R., Methods to obtain excellent capacity retention in LiCoO_2 cycled to 4.5 V. *Electrochimica Acta* **2004**, *49* (7), 1079-1090.
37. Lin, F.; Markus, I. M.; Nordlund, D.; Weng, T.-C.; Asta, M. D.; Xin, H. L.; Doeff, M. M., Surface reconstruction and chemical evolution of stoichiometric layered cathode materials for lithium-ion batteries. *Nature Communications* **2014**, *5*, 3529.
38. Liu, H.; Bugnet, M.; Tessaro, M. Z.; Harris, K. J.; Dunham, M. J. R.; Jiang, M.; Goward, G. R.; Botton, G. A., Spatially resolved surface valence gradient and structural transformation of lithium transition metal oxides in lithium-ion batteries. *Physical Chemistry Chemical Physics* **2016**, *18* (42), 29064-29075.
39. Yan, P.; Zheng, J.; Zhang, J.-G.; Wang, C., Atomic Resolution Structural and Chemical Imaging Revealing the Sequential Migration of Ni, Co, and Mn upon the Battery Cycling of Layered Cathode. *Nano Letters* **2017**, *17* (6), 3946-3951.
40. Zhou, Y.-N.; Ma, J.; Hu, E.; Yu, X.; Gu, L.; Nam, K.-W.; Chen, L.; Wang, Z.; Yang, X.-Q., Tuning charge–discharge induced unit cell breathing in layer-structured cathode materials for lithium-ion batteries. *Nature Communications* **2014**, *5*, 5381.
41. Kim, J.; Cho, H.; Jeong, H. Y.; Ma, H.; Lee, J.; Hwang, J.; Park, M.; Cho, J., Self-Induced Concentration Gradient in Nickel-Rich Cathodes by Sacrificial Polymeric Bead Clusters for High-Energy Lithium-Ion Batteries. *Advanced Energy Materials* **2017**, *7* (12), 1602559-n/a.
42. Yan, P.; Zheng, J.; Gu, M.; Xiao, J.; Zhang, J.-G.; Wang, C.-M., Intragranular cracking as a critical barrier for high-voltage usage of layer-structured cathode for lithium-ion batteries. *Nature Communications* **2017**, *8*, 14101.
43. Wang, H.; Jang, Y. I.; Huang, B.; Sadoway, D. R.; Chiang, Y. M., TEM Study of Electrochemical Cycling-Induced Damage and Disorder in LiCoO_2 Cathodes for Rechargeable Lithium Batteries. *Journal of The Electrochemical Society* **1999**, *146* (2), 473-480.
44. Kim, H.; Kim, M. G.; Jeong, H. Y.; Nam, H.; Cho, J., A New Coating Method for Alleviating Surface Degradation of $\text{LiNi}_0.6\text{Co}_0.2\text{Mn}_0.2\text{O}_2$ Cathode Material: Nanoscale Surface Treatment of Primary Particles. *Nano Letters* **2015**, *15* (3), 2111-2119.

45. Yan, P.; Zheng, J.; Chen, T.; Luo, L.; Jiang, Y.; Wang, K.; Sui, M.; Zhang, J.-G.; Zhang, S.; Wang, C., Coupling of electrochemically triggered thermal and mechanical effects to aggravate failure in a layered cathode. *Nature Communications* **2018**, *9* (1), 2437.
46. Cho, J.; Kim, Y. J.; Kim, T.-J.; Park, B., Zero-Strain Intercalation Cathode for Rechargeable Li-Ion Cell. *Angewandte Chemie International Edition* **2001**, *40* (18), 3367-3369.
47. Appapillai, A. T.; Mansour, A. N.; Cho, J.; Shao-Horn, Y., Microstructure of LiCoO₂ with and without “AlPO₄” Nanoparticle Coating: Combined STEM and XPS Studies. *Chemistry of Materials* **2007**, *19* (23), 5748-5757.
48. Shim, J.-H.; Lee, K.-S.; Missyul, A.; Lee, J.; Linn, B.; Lee, E. C.; Lee, S., Characterization of Spinel Li_xCo₂O₄-Coated LiCoO₂ Prepared with Post-Thermal Treatment as a Cathode Material for Lithium Ion Batteries. *Chemistry of Materials* **2015**, *27* (9), 3273-3279.
49. Liang, D. D.; Xiang, H. F.; Liang, X.; Cheng, S.; Chen, C. H., Spinel MgAl₂O₄ modification on LiCoO₂ cathode materials with the combined advantages of MgO and Al₂O₃ modifications for high-voltage lithium-ion batteries. *RSC Advances* **2017**, *7* (12), 6809-6817.
50. Jang, Y. I.; Huang, B.; Wang, H.; Sadoway, D. R.; Ceder, G.; Chiang, Y. M.; Liu, H.; Tamura, H., LiAl_yCo_{1-y}O₂ (R $\bar{3}m$) Intercalation Cathode for Rechargeable Lithium Batteries. *Journal of The Electrochemical Society* **1999**, *146* (3), 862-868.
51. Zhu, X.; Shang, K.; Jiang, X.; Ai, X.; Yang, H.; Cao, Y., Enhanced electrochemical performance of Mg-doped LiCoO₂ synthesized by a polymer-pyrolysis method. *Ceramics International* **2014**, *40* (7, Part B), 11245-11249.
52. Wang, Z.; Wang, Z.; Guo, H.; Peng, W.; Li, X., Improving the cycling stability of LiCoO₂ at 4.5V through co-modification by Mg doping and zirconium oxyfluoride coating. *Ceramics International* **2015**, *41* (1, Part A), 469-474.
53. Cho, W.; Myeong, S.; Kim, N.; Lee, S.; Kim, Y.; Kim, M.; Kang, S. J.; Park, N.; Oh, P.; Cho, J., Critical Role of Cations in Lithium Sites on Extended Electrochemical Reversibility of Co-Rich Layered Oxide. *Advanced Materials* **2017**, *29* (21), 1605578.
54. Kim, U. H.; Jun, D. W.; Park, K. J.; Zhang, Q.; Kaghazchi, P.; Aurbach, D.; Major, D. T.; Goobes, G.; Dixit, M.; Leifer, N.; Wang, C. M.; Yan, P.; Ahn, D.; Kim, K. H.; Yoon, C. S.; Sun, Y. K., Pushing the limit of layered transition metal oxide cathodes for high-energy density rechargeable Li ion batteries. *Energy & Environmental Science* **2018**, *11* (5), 1271-1279.
55. Park, K.-J.; Jung, H.-G.; Kuo, L.-Y.; Kaghazchi, P.; Yoon, C. S.; Sun, Y.-K., Improved Cycling Stability of Li[Ni_{0.90}Co_{0.05}Mn_{0.05}]O₂ Through Microstructure Modification by Boron Doping for Li-Ion Batteries. *Advanced Energy Materials* **2018**, *8* (25), 1801202.
56. Yoon, C. S.; Kim, U.-H.; Park, G.-T.; Kim, S. J.; Kim, K.-H.; Kim, J.; Sun, Y.-K., Self-Passivation of a LiNiO₂ Cathode for a Lithium-Ion Battery through Zr Doping. *ACS Energy Letters* **2018**, *3* (7), 1634-1639.
57. Wang, D. Y.; Sinha, N. N.; Petibon, R.; Burns, J. C.; Dahn, J. R., A systematic study of well-known electrolyte additives in LiCoO₂/graphite pouch cells. *Journal of Power Sources* **2014**, *251*, 311-318.
58. Ma, L.; Self, J.; Nie, M.; Glazier, S.; Wang, D. Y.; Lin, Y.-S.; Dahn, J. R., A systematic study of some promising electrolyte additives in Li[Ni_{1/3}Mn_{1/3}Co_{1/3}]O₂/graphite, Li[Ni_{0.5}Mn_{0.3}Co_{0.2}]/graphite and

Li[Ni_{0.6}Mn_{0.2}Co_{0.2}]/graphite pouch cells. *Journal of Power Sources* **2015**, 299, 130-138.

59. Liu, Q.; Su, X.; Lei, D.; Qin, Y.; Wen, J.; Guo, F.; Wu, Y. A.; Rong, Y.; Kou, R.; Xiao, X.; Aguesse, F.; Bareño, J.; Ren, Y.; Lu, W.; Li, Y., Approaching the capacity limit of lithium cobalt oxide in lithium ion batteries via lanthanum and aluminium doping. *Nature Energy* **2018**.
60. Vetter, J.; Novák, P.; Wagner, M. R.; Veit, C.; Möller, K. C.; Besenhard, J. O.; Winter, M.; Wohlfahrt-Mehrens, M.; Vogler, C.; Hammouche, A., Ageing mechanisms in lithium-ion batteries. *Journal of Power Sources* **2005**, 147 (1), 269-281.
61. Dedryvère, R.; Martinez, H.; Leroy, S.; Lemordant, D.; Bonhomme, F.; Biensan, P.; Gonbeau, D., Surface film formation on electrodes in a LiCoO₂/graphite cell: A step by step XPS study. *Journal of Power Sources* **2007**, 174 (2), 462-468.
62. Chen, X.; Xu, W.; Xiao, J.; Engelhard, M. H.; Ding, F.; Mei, D.; Hu, D.; Zhang, J.; Zhang, J.-G., Effects of cell positive cans and separators on the performance of high-voltage Li-ion batteries. *Journal of Power Sources* **2012**, 213, 160-168.
63. Maeyoshi, Y.; Miyamoto, S.; Munakata, H.; Kanamura, K., Enhanced cycle stability of LiCoPO₄ by using three-dimensionally ordered macroporous polyimide separator. *Journal of Power Sources* **2017**, 350, 103-108.

